

Distribution Category:  
Energy Conversion  
(UC-93)A

ANL-84-64

ANL--84-64

DE85 009662

**DISCLAIMER**

This report was prepared as an account of work sponsored by an agency of the United States Government. Neither the United States Government nor any agency thereof, nor any of their employees, makes any warranty, express or implied, or assumes any legal liability or responsibility for the accuracy, completeness, or usefulness of any information, apparatus, product, or process disclosed, or represents that its use would not infringe privately owned rights. Reference herein to any specific commercial product, process, or service by trade name, trademark, manufacturer, or otherwise does not necessarily constitute or imply its endorsement, recommendation, or favoring by the United States Government or any agency thereof. The views and opinions of authors expressed herein do not necessarily state or reflect those of the United States Government or any agency thereof.

ARGONNE NATIONAL LABORATORY  
9700 South Cass Avenue  
Argonne, Illinois 60439

**ADVANCED FUEL CELL DEVELOPMENT**

Progress Report for

January-March 1984

by

R. D. Pierce, B. Baumert,\* T. D. Claar,† R. J. Fousek,† H. S. Huang,  
T. D. Kaun, M. Krumpelt, N. Q. Minh, F. C. Mrazek, R. B. Poeppel,†  
J. L. Smith, J. R. Stapay, J. Emerson,†  
S. A. Zwick, and D. C. Fee

Chemical Technology Division

January 1985

Previous reports in this series

ANL-83-89	April-June 1983
ANL-84-9	July-September 1983
ANL-84-38	October-December 1983

**MASTER**

\* Student Research Participant from Indiana University of Pennsylvania.

† Materials Science and Technology Division, ANL.

## TABLE OF CONTENTS

	<u>Page</u>
ABSTRACT . . . . .	1
SUMMARY . . . . .	1
I. INTRODUCTION . . . . .	4
II. CATHODE DEVELOPMENT . . . . .	5
A. Conductivity of Alternative Cathode Materials . . . . .	5
1. $\text{Li}_2\text{MnO}_3$ . . . . .	5
2. $\text{LiFeO}_2$ . . . . .	9
B. Solubility of Alternative Cathode Materials . . . . .	17
1. $\text{NiO}$ . . . . .	17
2. Zirconium-Doped $\text{ZnO}$ and $\text{ZrO}_2$ . . . . .	18
3. Magnesium-Doped $\text{Li}_2\text{MnO}_3$ . . . . .	19
4. $\text{LiFeO}_2$ . . . . .	20
C. Effect of Gas Pressure upon Cathode Material Solubility . . .	20
D. Cathode Material Migration . . . . .	23
III. COMPONENT STRUCTURE DEVELOPMENT AND EVALUATION . . . . .	25
A. Cathode Structure Development . . . . .	25
B. Evaluation of Anode Creep Resistance . . . . .	29
IV. GAS CLEANUP SYSTEM ANALYSIS . . . . .	32
V. MODEL DEVELOPMENT FOR SOLID OXIDE FUEL CELL . . . . .	39
REFERENCES . . . . .	42

## LIST OF FIGURES

<u>No.</u>	<u>Title</u>	<u>Page</u>
1.	Resistivity of Mg-Doped $\text{Li}_2\text{MnO}_3$ from Batches LMM1, LMM3A, LMM3B, and 247-133/141 . . . . .	5
2.	Resistivity of Mg-Doped $\text{Li}_2\text{MnO}_3$ from Batches LMM3A and LMM3B . . . . .	6
3.	Resistivity of Mg-Doped $\text{Li}_2\text{MnO}_3$ from Batch 247-139/141 . . . . .	7
4.	Resistivities of Six $\text{Li}_2\text{MnO}_3$ Samples Treated in $2/3 \text{ CO}_2$ - $1/3 \text{ O}_2$ for 100 h at $700^\circ\text{C}$ . . . . .	7
5.	Resistivity of Undoped $\text{Li}_2\text{MnO}_3$ for Pellets 283-1-2 and 283-1-4 . . . . .	8
6.	Resistivity of Undoped and Mg-Doped $\text{Li}_2\text{MnO}_3$ Prepared under $1/3 \text{ O}_2$ - $2/3 \text{ CO}_2$ . . . . .	9
7.	Resistivity of Mn-Doped $\text{LiFeO}_2$ . . . . .	10
8.	Resistivity of Zr-Doped $\text{LiFeO}_2$ . . . . .	12
9.	Resistivity of Ni-Doped $\text{LiFeO}_2$ . . . . .	13
10.	Resistivity of Cu-Doped $\text{LiFeO}_2$ . . . . .	14
11.	Resistivity of Undoped $\text{LiFeO}_2$ Prepared at $600^\circ\text{C}$ . . . . .	15
12.	Resistivity of Undoped $\text{LiFeO}_2$ Prepared under $2/3 \text{ CO}_2$ - $1/3 \text{ O}_2$ . . . . .	16
13.	Resistivity of Undoped $\text{LiFeO}_2$ Prepared under 30% $\text{CO}_2$ -70% $\text{O}_2$ . . . . .	17
14.	Solubilities of NiO and Alternative Cathode Materials as a Function of Temperature . . . . .	18
15.	Zinc Concentration Levels due to Dissolution of Zirconium-Doped ZnO as a Function of Temperature . . . . .	19
16.	Iron Levels due to Solubility of $\text{LiFeO}_2$ as a Function of Temperature . . . . .	20
17.	Arrangement of Samples for Studies of the Cathode Gas Pressure Effect . . . . .	21

# LIST OF FIGURES (contd)

<u>No.</u>	<u>Title</u>	<u>Page</u>
18.	Solubility Apparatus for Examining Cathode Gas Pressure Effects at 1 atm . . . . .	22
19.	Scanning Electron Micrographs of Organic Pore Formers Used in Tape Cast $\text{Li}_2\text{MnO}_3$ -Mg Cathodes . . . . .	27
20.	Scanning Electron Micrographs of Mg-Doped $\text{Li}_2\text{MnO}_3$ Tapes Sintered 1 h at 1250°C in Air. . . . .	28
21.	Schematic of Apparatus Used to Monitor Thermomechanical Behavior . . . . .	30
22.	Compression Cage for Anode Creep Tests Assembled and Disassembled . . . . .	31
23.	Effect of Bleed-Off and Sulfur Contents on Plant Efficiency at 80% Fuel Utilization (1 ppm eq. $\text{H}_2\text{S}$ corresponds to 10 mV voltage drop) . . . . .	32
24.	Effect of Bleed-Off and Sulfur Contents on Plant Efficiency at 80% Fuel Utilization (1 ppm eq. $\text{H}_2\text{S}$ corresponds to 15 mV voltage drop) . . . . .	33
25.	Effect of Bleed-Off and Sulfur Contents on Plant Efficiency at 80% Fuel Utilization (1 ppm eq. $\text{H}_2\text{S}$ corresponds to 20 mV voltage drop) . . . . .	33
26.	Effect of Bleed-Off and Sulfur Contents on Plant Efficiency at 85% Fuel Utilization (1 ppm eq. $\text{H}_2\text{S}$ corresponds to 10 mV voltage drop) . . . . .	34
27.	Effect of Bleed-Off and Sulfur Contents on Plant Efficiency at 85% Fuel Utilization (1 ppm eq. $\text{H}_2\text{S}$ corresponds to 15 mV voltage drop) . . . . .	34
28.	Effect of Bleed-Off and Sulfur Contents on Plant Efficiency at 85% Fuel Utilization (1 ppm eq. $\text{H}_2\text{S}$ corresponds to 20 mV voltage drop) . . . . .	35
29.	Effect of Bleed-Off and Sulfur Contents on Plant Efficiency at 90% Fuel Utilization (1 ppm eq. $\text{H}_2\text{S}$ corresponds to 10 mV voltage drop) . . . . .	35
30.	Effect of Bleed-Off and Sulfur Contents on Plant Efficiency at 90% Fuel Utilization (1 ppm eq. $\text{H}_2\text{S}$ corresponds to 15 mV voltage drop) . . . . .	36

# LIST OF FIGURES (contd)

<u>No.</u>	<u>Title</u>	<u>Page</u>
31.	Effect of Bleed-Off and Sulfur Contents on Plant Efficiency at 90% Fuel Utilization (1 ppm eq. H <sub>2</sub> S corresponds to 20 mV voltage drop) . . . . .	36
32.	Effect of Fuel Utilization and Sulfur Contents on Plant Efficiency at 10% Bleed-Off . . . . .	37
33.	Temperature Profile along the Length of a Solid Oxide Fuel Cell . . . . .	41

# LIST OF TABLES

<u>No.</u>	<u>Title</u>	<u>Page</u>
1.	Properties of $\text{Li}_2\text{MnO}_3$ Samples . . . . .	8
2.	Properties of Mn-Doped $\text{LiFeO}_2$ Samples . . . . .	10
3.	Properties of Zr-Doped $\text{LiFeO}_2$ Samples . . . . .	11
4.	Properties of Ni-Doped $\text{LiFeO}_2$ Prepared by Coprecipitation . . . .	12
5.	Properties of Cu-Doped $\text{LiFeO}_2$ Samples . . . . .	14
6.	Properties of Undoped $\text{LiFeO}_2$ Prepared at $600^\circ\text{C}$ . . . . .	15
7.	Properties of Undoped $\text{LiFeO}_2$ Prepared under Different Gas Atmospheres . . . . .	16
8.	Electrolyte Analysis for Selected Cations . . . . .	23
9.	Summary of $\text{Li}_2\text{MnO}_3$ Tape Casting Experiments . . . . .	26
10.	Magnesium-Doped $\text{Li}_2\text{MnO}_3$ Tapes Sintered 1 h at $1250^\circ\text{C}$ in Air . . .	29

## ADVANCED FUEL CELL DEVELOPMENT

Progress Report for  
January-March 1984

by

R. D. Pierce, B. Baumert,\* T. D. Claar,† R. J. Fousek,† H. S. Huang,  
T. D. Kaun, M. Krumpelt, N. O. Minh, F. C. Mrazek, R. B. Poeppel,†  
J. L. Smith, J. R. Stapay, J. Emerson,†  
S. A. Zwick, and D. C. Fee

### ABSTRACT

This report describes fuel cell research and development activities at Argonne National Laboratory (ANL) during the period January through March 1984. These efforts have been directed principally toward seeking alternative cathode materials to NiO for molten carbonate fuel cells. Based on an investigation of the thermodynamically stable phases formed under cathode conditions, a number of prospective alternative cathode materials have been identified. From the list of candidates,  $\text{LiFeO}_2$ ,  $\text{Li}_2\text{MnO}_3$ , and  $\text{ZnO}$  were selected for further investigation. During this quarter, they were doped to promote conductivity and tested for solubility and ion migration in the cell environment. These tests showed that  $\text{Li}_2\text{MnO}_3$  and  $\text{LiFeO}_2$  are attractive, but work is being done to better understand the conductivity of these materials;  $\text{ZnO}$  has proved to be too soluble for further consideration.

An investigation directed to understanding in-cell densification of anode materials was initiated. In addition, calculations were made to evaluate the practicality of controlling sulfur accumulation in molten carbonate fuel cells by bleed-off of a portion of the anode gas that could be recycled to the cathode.

In addition, a model is being developed to predict the performance of solid oxide fuel cells as a function of cell design and operation.

### SUMMARY

Because the dissolution of NiO cathodes appears to be excessive for pressurized molten carbonate fuel cells (MCFC), the major research activity at ANL in support of DOE's MCFC program has been directed to finding a more stable cathode material. In addition, an effort has been initiated to assess densification mechanisms for MCFC anodes.

---

\*Student Research Participant from Indiana University of Pennsylvania.

†Materials Science and Technology Division, ANL.

## Cathode Development

Conductivity of Alternative Cathode Materials. Two materials,  $\text{Li}_2\text{MnO}_3$  and  $\text{LiFeO}_2$ , previously identified as stable in the cathode environment, were tested for conductivity. A number of  $\text{Li}_2\text{MnO}_3$  samples, either undoped or magnesium-doped, were prepared and are being analyzed in an effort to learn why conductivity has varied excessively from batch to batch. The effect on the conductivity of oxygen and  $\text{CO}_2$  partial pressures during the synthesis steps will be studied.

Similarly, the conductivity of batches of undoped and doped  $\text{LiFeO}_2$  is being studied. Manganese, copper, zirconium, and nickel were used as dopants. A strong influence of cover-gas composition during synthesis was observed, but little effect of dopant on conductivity was found. Samples prepared under gas containing  $\text{CO}_2$  have higher resistivities than those prepared under air.

Solubility of Alternative Cathode Materials. Solubility data were obtained for samples of  $\text{NiO}$ ,  $\text{Li}_2\text{MnO}_3$ ,  $\text{LiFeO}_2$ , and  $\text{ZnO}$ . Data were taken with the candidate material combined with different  $\text{Li}_2\text{CO}_3$ - $\text{K}_2\text{CO}_3$  mixtures (62 mol %  $\text{Li}_2\text{CO}_3$  and 70 mol %  $\text{Li}_2\text{CO}_3$ ). Measured  $\text{NiO}$  solubilities were lower in the 70 mol %  $\text{Li}_2\text{CO}_3$ - $\text{K}_2\text{CO}_3$  salt ( $\sim 1$  ppmW at 925 K). In addition,  $\text{NiO}$  solubilities with 70 mol %  $\text{Li}_2\text{CO}_3$  were less sensitive to the moisture content of the cover gas than they were with 62 mol %  $\text{Li}_2\text{CO}_3$ .

The solubility of  $\text{ZnO}$  was excessive in both salt mixtures, but zirconium dopant solubility was below the detection limits ( $< 1$  ppmW). The  $\text{Li}_2\text{MnO}_3$  solubilities were low ( $\sim 1$  ppmW at  $700^\circ\text{C}$  in 70 mol %  $\text{Li}_2\text{CO}_3$ ), but data for magnesium-doped samples indicate unsuccessful incorporation of the dopant, resulting in high magnesium levels in the salt. The solubility of  $\text{LiFeO}_2$  increases somewhat with moist gas and in going from the 62 mol % to the 70 mol %  $\text{Li}_2\text{CO}_3$  salt, but the solubility level remains attractive ( $\sim 10$  ppmW iron).

An effort has been initiated to determine solubilities under pressurized conditions.

Cathode Materials Migration. Additional cell tests were made to assess migration from cathodes of  $\text{LiFeO}_2$  and magnesium-doped  $\text{Li}_2\text{MnO}_3$ . Iron and manganese migration remained low, but magnesium migration was high because of poor incorporation of the dopant into the  $\text{Li}_2\text{MnO}_3$  lattice.

## Component Structure Development and Evaluation

Cathode Structure Development. Work has continued on development of cathode structures for testing alternative cathode materials. Tapes were prepared of magnesium-doped  $\text{Li}_2\text{MnO}_3$  with and without pore formers. Porosities range from about 50% for sintered samples without pore formers to 84% for unfired samples with pore formers. Mercury porosimetry is being performed to determine pore size distributions. Many tapes were fired for analysis, but unfired tapes are recommended for cathode application.



Evaluation of Anode Creep Resistance. A new activity was initiated to improve the understanding of anode creep and densification occurring under fuel cell conditions. Where possible, anodes under development by industrial contractors will be examined, tested, and assessed on a consistent basis. Test apparatus used earlier for thermomechanical testing of electrolyte structures is being modified for compression testing of anodes.

#### Gas Cleanup System Analysis

Calculations were made to evaluate the practicality of controlling sulfur buildup in MCFC stacks using natural gas feed by bleeding off a portion of the anode exhaust that would otherwise be recycled to the cathode. Although the technique provides a removal path for sulfur to improve performance, it also affects cell performance by lowering the CO<sub>2</sub> content of the cathode gas. Peak efficiencies are indicated at a bleed-off ratio of about 10%, but a loss in overall plant efficiency of 3 to 8% as compared to 100% recycle and sulfur-free gas is indicated.

#### Model Development for Solid Oxide Fuel Cells

A model is being developed to predict the effect on performance of solid oxide fuel cells (SOFC) arising from changes in cell design and operation. The current SOFC model incorporates the basic cell thermodynamics, cell resistance, and heat transfer processes. Calculations with the model were made to determine the effect on cell operating temperature of internal vs. external reform of fuel.

## I. INTRODUCTION

The advanced fuel cell studies at ANL are part of the DOE Advanced Fuel Cell Program. The objective of this DOE program is to reduce the technical uncertainties with fuel cells so that manufacturers and users can introduce high-efficiency generating systems, which have the capability of operating on coal or other fuels. At the present stage of development, the primary thrust of the ANL program is to provide supporting research and development that pursues fundamental understanding of fuel cell behavior and investigates alternative stack concepts.

The present molten carbonate fuel cells consist of a porous nickel anode, a porous lithiated nickel oxide cathode, an electrolyte structure that separates the anode and cathode and conducts only ionic current between them, and appropriate metal housings or, in the case of stacks of cells, intercell separator sheets. The cell housings (or separator sheets) bear upon the electrolyte structure to form a seal between the environment and the anode and cathode gas compartments. The usual electrolyte structure is a composite of discrete  $\text{LiAlO}_2$  particles and a mixture of alkali metal carbonates. The carbonates are liquid at the cell operating temperature of about  $650^\circ\text{C}$  (925 K). At the anode, hydrogen and carbon monoxide in the fuel gas react with carbonate ion from the electrolyte to form water and carbon dioxide while giving up electrons to the external circuit. At the cathode, carbon dioxide and oxygen react and accept electrons from the external circuit to form carbonate ion, which is conducted through the electrolyte to the anode. In a practical cell stack,  $\text{CO}_2$  for the cathode probably would be obtained from the anode exhaust.

It has become apparent that for pressurized operation, which is desirable for large power plants, nickel dissolution from the  $\text{NiO}$  cathode and deposition of metallic nickel in the electrolyte will prevent the attainment of the  $4 \times 10^4$  h lifetime desired for commercial cells. The evaluation of possible alternative cathode materials is our principal current activity. We are also investigating anode densification mechanisms.

Work is under way to develop a model of solid oxide fuel cell performance. The solid oxide fuel cell consists of a lanthanum manganate cathode, a zirconium dioxide electrolyte, a cermet anode, and lanthanum chromite for electronic cell-to-cell interconnections.

## II. CATHODE DEVELOPMENT

### A. Conductivity of Alternative Cathode Materials (J. L. Smith, N. Q. Minh)

Because of the problem of NiO cathode dissolution in molten carbonate fuel cells, the experimental work at ANL is concentrated principally on the investigation of alternative cathode materials. Currently, attention is focused on testing of  $\text{LiFeO}_2$  and  $\text{Li}_2\text{MnO}_3$  and the effect of synthesis conditions on the resistivity of these materials in their doped and undoped states.

#### 1. $\text{Li}_2\text{MnO}_3$ (J. L. Smith, N. Q. Minh)

Conductivities of several batches of  $\text{Li}_2\text{MnO}_3$  were measured. Results for three samples of Mg-doped material ( $\text{Mg}/\text{Mn} = 1/10$ ) synthesized at ANL's Materials Science and Technology Division (MST) (ANL-84-38, p. 30) are shown in Fig. 1. These materials were reacted with stoichiometric amounts of  $\text{Li}_2\text{CO}_3$  in air. Also shown in Fig. 1 is the conductivity of a material with the same  $\text{Mg}/\text{Mn}$  ratio but reacted in 30%  $\text{CO}_2$ -air and with excess carbonate eutectic.

Because of problems with producing low-resistivity  $\text{Li}_2\text{MnO}_3$ , we decided to spend full time reacting batches of the material under various gaseous conditions (at 1 atm) in order to ascertain their effect on conductivity. At present, five batches of Mn/Mg oxides have been made. Three of these are dry preparations, i.e.,  $\text{Mn}_2\text{O}_3 + \text{MgO}$  mixed and heat treated. The Mn/Mg ratios are nominally 5/1, 10/1, and 15/1. One is a coprecipitation preparation with  $\text{Mn}/\text{Mg} = 10/1$ . Finally, there will be a batch of undoped manganese oxide. All subsequent processing will be done in 1-atm air.

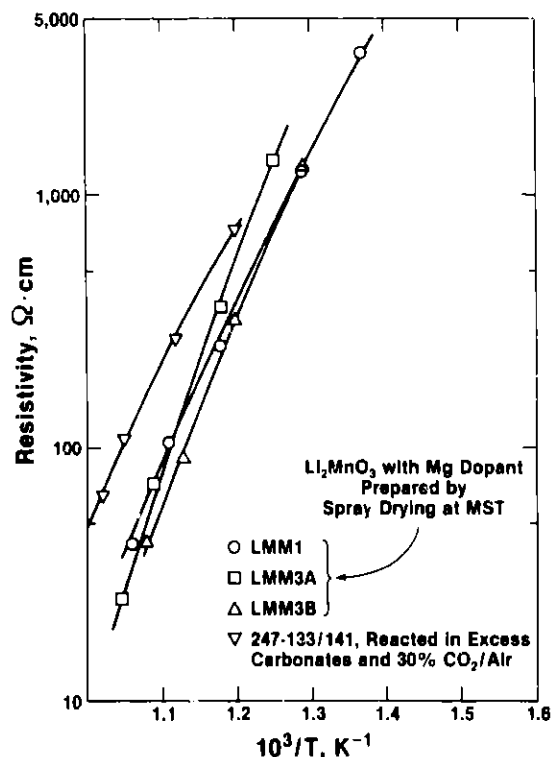


Fig. 1.

Resistivity of Mg-Doped  
 $\text{Li}_2\text{MnO}_3$  from Batches  
LMM1, LMM3A, LMM3B, and  
247-133/141

These five starting materials will be reacted with carbonates under controlled gaseous environments. By mixing  $N_2$ ,  $CO_2$ , and  $O_2$ , the oxygen partial pressure will be varied with the carbon dioxide partial pressure remaining constant, and then the carbon dioxide partial pressure will be varied with the oxygen partial pressure remaining constant. The samples will be sintered and tested for conductivity.

Figure 2 is a plot of the results for the powders LMM3A and LMM3B, which were produced by a spray-drying process (ANL-84-38, p. 33) and reacted with stoichiometric amounts of  $Li_2CO_3$  in air. The solid line is for pellets of the powders as reacted in air, and the dashed lines represent data for pellets from powders reacted in air with subsequent heat treatment for 100 h at  $700^\circ C$  in  $2/3 CO_2$ - $1/3 O_2$ . Figure 3 shows resistivity data for batch 247-139/141, a coprecipitated material with  $Mn/Mg = 10/1$ . The solid line represents the resistivity for material that was reacted at  $700^\circ C$  for 100 h in 30%  $CO_2$ -balance air, the dashed line is for  $2/3 CO_2$ - $1/3 O_2$ . Figure 4 gives resistivity data for a number of materials reacted at  $700^\circ C$  for 100 h in  $2/3 CO_2$ - $1/3 O_2$ ; the nominal dopant ratio ( $Mn/Mg$ ) for the 151-1, -2, and -3 samples is 5/1, 10/1 and 15/1, respectively.

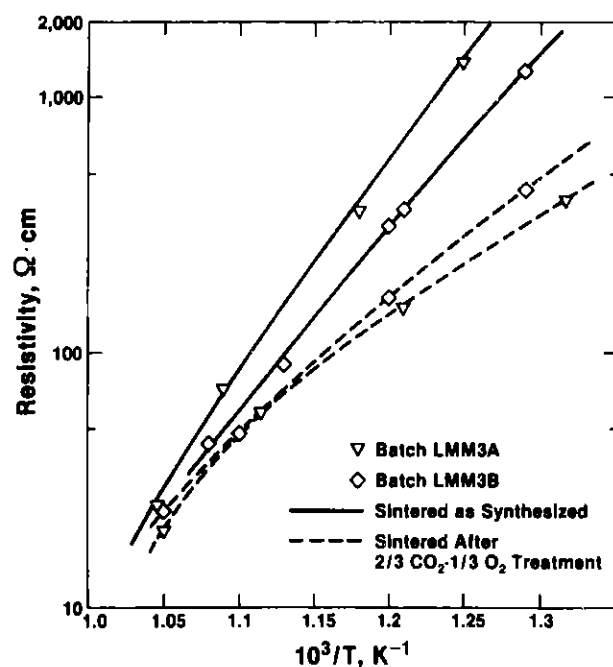


Fig. 2.

Resistivity of Mg-Doped  
 $Li_2MnO_3$  from Batches  
LMM3A and LMM3B

It is premature to draw conclusions from these data because a number of factors cannot be precisely controlled. Although the data for the LMM3A, LMM3B, and the 247-139/141 pellets suggest that gaseous environment is the controlling factor for resistivity, caution must be taken in drawing such a conclusion; variations in sintering, for example, could be the dominant factor affecting resistivity. The data for the 151-1, -2, -3 pellets suggest dopant is not a factor, but dopant incorporation is an unknown variable. More experiments in this vein will be done.

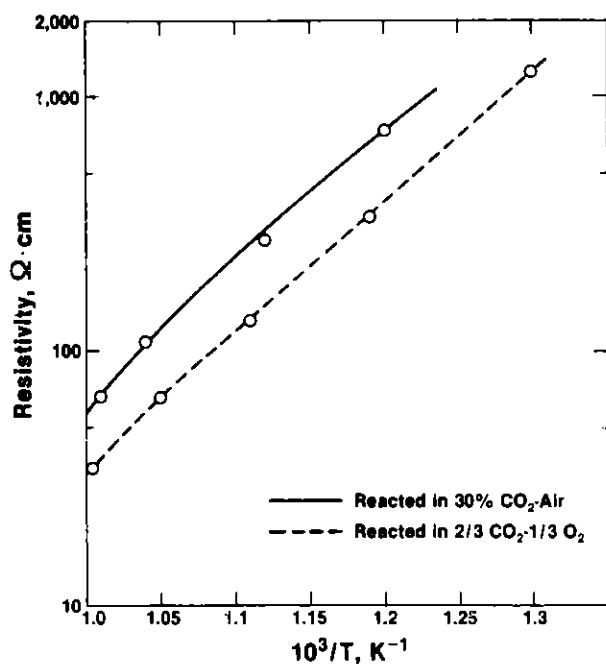


Fig. 3.

Resistivity of Mg-Doped  
 $\text{Li}_2\text{MnO}_3$  from Batch  
 247-139/141

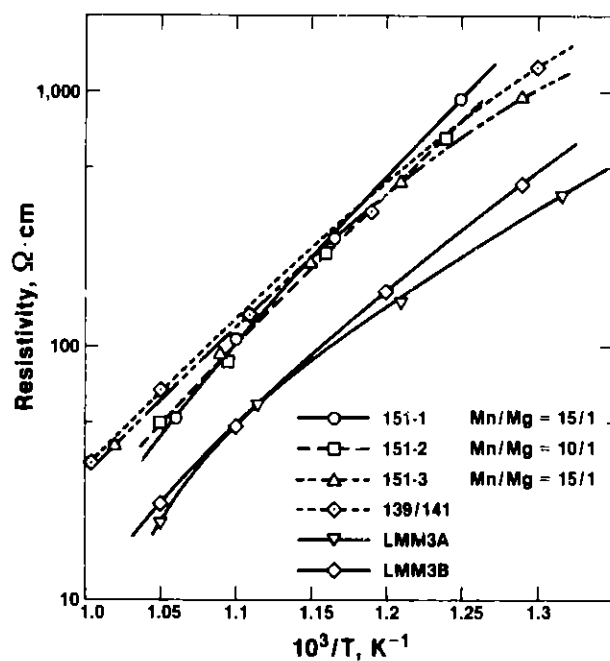


Fig. 4.

Resistivities of Six  $\text{Li}_2\text{MnO}_3$   
 Samples Treated in  $2/3 \text{ CO}_2$ -  
 $1/3 \text{ O}_2$  for 100 h at  $700^\circ\text{C}$

Table 1 and Figs. 5 and 6 are compilations of data for some other samples of  $\text{Li}_2\text{MnO}_3$ . Figure 5 shows data for two undoped  $\text{Li}_2\text{MnO}_3$  samples. As indicated by Table 1, Sample 283-1-2 has significant  $\text{LiMnO}_2$  present, possibly accounting for the resistivity curve in Fig. 5. Figure 6 shows data for a doped sample (283-M1-2) and the undoped sample (283-1-4) shown in Fig. 5. Again, X-ray diffraction shows  $\text{LiMnO}_2$ . The presence of  $\text{LiMnO}_2$  may be due to an incomplete reaction step or it may be indicative of changes during sintering.

Table 1. Properties of  $\text{Li}_2\text{MnO}_3$  Samples

Pellet No.	Gas Atmosphere in the Carbonate Treatment	Sintered Pellet	XRD before Sintering*
283-1-2. (Undoped)	Air	87% dense	Well crystalline $\text{Li}_2\text{MnO}_3$ + minor $\text{LiMnO}_2$
283-1-4 (Undoped)	1/3 $\text{O}_2$ -2/3 $\text{CO}_2$	87% dense	Well crystalline $\text{Li}_2\text{MnO}_3$
283-M1-2 (Mg-doped)	1/3 $\text{O}_2$ -2/3 $\text{CO}_2$	70% dense	$\text{LiMnO}_2$ , $\text{Li}_2\text{MnO}_3$

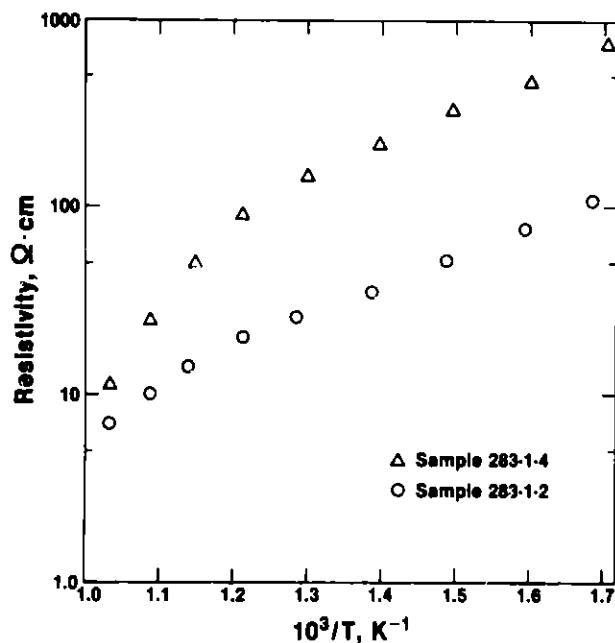


Fig. 5.

Resistivity of Undoped  $\text{Li}_2\text{MnO}_3$  for Pellets 283-1-2 and 283-1-4

A  $\text{Li}_2\text{MnO}_3$  sample prepared by solids mixing has been shown conclusively to have incomplete mixing. Particles with Mg and without Mn were found by scanning electron microscopy/energy dispersive X-ray (SEM-EDS) analyses. Furthermore, in a selective washing process (see Section II.B.3), most of the Mg in the sample was removed.

The observed resistivity variation among the  $\text{Li}_2\text{MnO}_3$  samples can be attributed to variations in the degree of dopant incorporation and/or variations in stoichiometry. Variations in stoichiometry can, in turn, result from variations in reaction conditions, changes during sintering, and/or equilibration during the conductivity measurement. Minor variations in resistivity

\* All X-ray diffraction data given in this report obtained by B. S. Tani, ANL's Analytical Chemistry Laboratory.

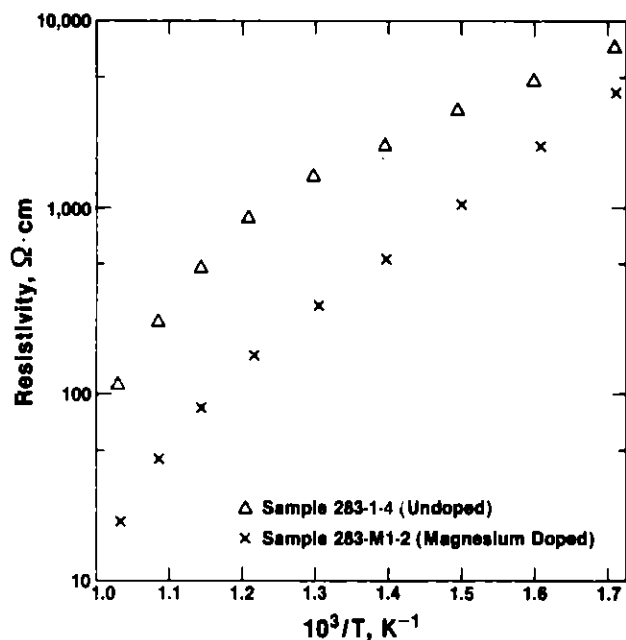


Fig. 6.

Resistivity of Undoped and  
Mg-Doped  $Li_2MnO_3$  Prepared  
under  $1/3 O_2$ - $2/3 CO_2$

can occur due to pellet density variation, but these alone should not cause activation energy changes (i.e., changes in the slope of the log resistivity vs.  $1/T$  plot). The dominant mechanism affecting resistivity may vary among different samples.

As stated earlier, evidence of incomplete dopant incorporation has been observed in some  $Li_2MnO_3$  samples. Moreover, variations in resistivity were attributed to reaction conditions when large batches were made. A probable cause of resistivity variation was sintering, as evidenced by sample color changes. In one instance, about a 20% change in resistivity was observed during equilibration in the conductivity apparatus.

## 2. $LiFeO_2$ (N. Q. Minh)

The effects of dopant and material preparation conditions are currently under investigation for  $LiFeO_2$ . In the last quarterly, attention centered on examining the effect of preparation parameters such as temperature, carbonate salt composition, and gas atmosphere on the resistivity of Mn-doped and undoped  $LiFeO_2$ . It was found that samples prepared at  $700^\circ C$  under  $CO_2$ -air show much higher resistivity than those prepared under air. Carbonate salt composition appeared to have an effect at higher temperatures. For example, the resistivity of  $LiFeO_2$  prepared with excess  $Li_2CO_3$  or  $Li_2CO_3$ - $K_2CO_3$  eutectic under air at  $850^\circ C$  was much higher than that prepared with stoichiometric  $Li_2CO_3$ . No such effect was observed for materials prepared at  $700^\circ C$ . Although manganese doping ( $Fe/Mn = 5/1$ ) produced a marked reduction in lattice parameter for  $LiFeO_2$ , it had a small effect on the resistivity. During this reporting period, the resistivity of  $LiFeO_2$  doped with lower manganese concentration ( $Fe/Mn$  ratio =  $10/1$ ) was determined, and a series of Zr-doped, Ni-doped, and Cu-doped  $LiFeO_2$  samples was prepared and tested for conductivity. Syntheses of several undoped  $LiFeO_2$  samples were also carried out under different gas atmospheres, and the resistivities of the samples were measured using the van der Pauw technique.

The experimental procedure used to prepare Mn-doped  $\text{LiFeO}_2$  with a Fe/Mn ratio of 10/1 was identical to that described earlier (ANL-84-9, p. 5). Details of the preparation parameters and X-ray diffraction results for two Mn-doped pellets are summarized in Table 2.

Table 2. Properties of Mn-Doped  $\text{LiFeO}_2$  Samples

Sample No.	Carbonate Treatment			XRD before Sintering
	Carbonate	Temp.	Gas	
FM-4P3	Stoichiometric $\text{Li}_2\text{CO}_3$	700°C	30% $\text{CO}_2$ -air	$a = 4.152 \text{ \AA}$
FM-4P4	$\text{Li}_2\text{CO}_3\text{-K}_2\text{CO}_3$	700°C	30% $\text{CO}_2$ -air	$a = 4.152 \text{ \AA}$

The resistivity data are shown in Fig. 7, where it can be seen that carbonate composition (stoichiometric  $\text{Li}_2\text{CO}_3$  or  $\text{Li}_2\text{CO}_3\text{-K}_2\text{CO}_3$  eutectic) used in the carbonate treatment of the coprecipitated material had no effect on the resistivity of the prepared Mn-doped samples. The X-ray diffraction data indicate a decrease in lattice parameter, 4.152 Å for the Mn-doped  $\text{LiFeO}_2$  as compared with 4.158 Å for undoped  $\text{LiFeO}_2$ . The decrease in lattice constant for these Mn-doped samples (Fe/Mn = 10/1) is somewhat smaller than that for samples doped with higher Mn concentrations (Fe/Mn ratio of 5/1). A lattice constant of about 4.144 Å was observed for Mn-doped  $\text{LiFeO}_2$  with an Fe/Mn ratio of 5/1 (ANL-84-38, p. 6). Therefore, the lattice parameter for  $\text{LiFeO}_2$  appears to decrease with increasing manganese dopant content. Although a smaller lattice parameter is observed, Fig. 7 indicates that Mn doping at this concentration level (Fe/Mn = 10/1) did not lead to any noticeable change in the resistivity of  $\text{LiFeO}_2$ .

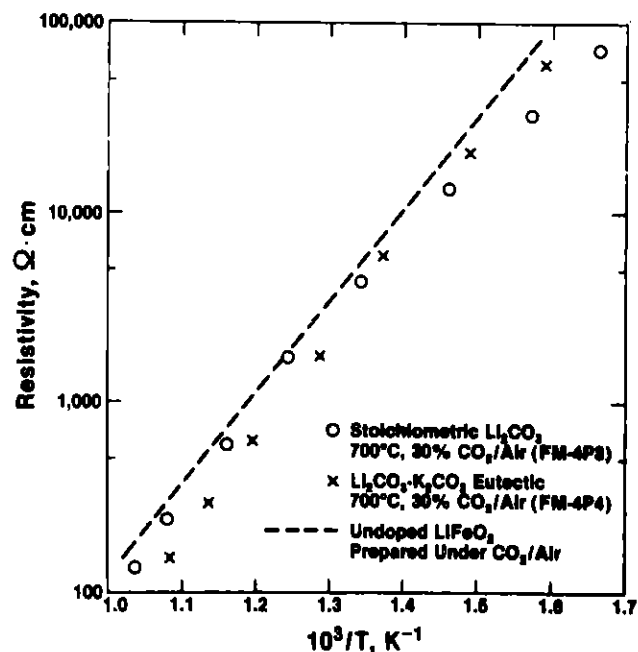


Fig. 7.

Resistivity of Mn-Doped  $\text{LiFeO}_2$  (Fe/Mn = 10/1)



A series of Zr-doped  $\text{LiFeO}_2$  samples (nominal  $\text{Fe/Zr} = 20/1$ ) was prepared. The zirconium-doped material was prepared by reacting zirconium and iron coprecipitate with carbonate salt. The reaction was carried out at  $700^\circ\text{C}$  under air or 30%  $\text{CO}_2$ -air, using stoichiometric amount of  $\text{Li}_2\text{CO}_3$  or  $\text{Li}_2\text{CO}_3$ - $\text{K}_2\text{CO}_3$  eutectic (Table 3).

Table 3. Properties of Zr-Doped  $\text{LiFeO}_2$  Samples

Sample No.	Carbonate Treatment			XRD before Sintering
	Carbonate	Temp.	Gas	
FZ-1P1	Stoichiometric $\text{Li}_2\text{CO}_3$	$700^\circ\text{C}$	Air	$a = 4.164 \text{ \AA}$
FZ-1P2	$\text{Li}_2\text{CO}_3$ - $\text{K}_2\text{CO}_3$	$700^\circ\text{C}$	Air	$a = 4.163 \text{ \AA}$
FZ-1P3	Stoichiometric $\text{Li}_2\text{CO}_3$	$700^\circ\text{C}$	30% $\text{CO}_2$ /air	$a = 4.168 \text{ \AA}$
FZ-1P4	$\text{Li}_2\text{CO}_3$ - $\text{K}_2\text{CO}_3$	$700^\circ\text{C}$	30% $\text{CO}_2$ /air	$a = 4.160 \text{ \AA} +$ very minor $\text{ZrO}_2$

The results of X-ray diffraction analysis of the prepared Zr-doped material, shown in Table 3, indicate that zirconium doping produced an increase in lattice constant for  $\text{LiFeO}_2$ . Figure 8 shows the electrical resistivity of Zr-doped  $\text{LiFeO}_2$  as a function of temperature. As in the cases of undoped  $\text{LiFeO}_2$  and Mn-doped  $\text{LiFeO}_2$  ( $\text{Fe/Mn} = 5/1$ ), Zr-doped material synthesized with stoichiometric amounts of  $\text{Li}_2\text{CO}_3$  under air yielded the lowest resistivity; much higher resistivities were observed for materials prepared with excess carbonate eutectic or in  $\text{CO}_2$ /air atmosphere.

The experimental procedure used to prepare Ni-doped  $\text{LiFeO}_2$  is similar to that described for Mn doping (ANL-84-38, p. 5). In this preparation, however,  $\text{LiOH}$  solution was used instead of ammonia solution because nickel forms soluble complexes with ammonia. Details of the preparation conditions and X-ray diffraction results for prepared material are shown in Table 4.

These X-ray diffraction results show a smaller lattice parameter for the Ni-doped samples prepared under air with stoichiometric amounts of  $\text{Li}_2\text{CO}_3$ . The samples prepared under  $\text{CO}_2$ -air were identified as  $\text{LiFeO}_2$  with a lattice constant of  $4.158 \text{ \AA}$ , the literature value for undoped  $\text{LiFeO}_2$  ( $\text{LiFe}_5\text{O}_8$  as a very minor phase was also observed for sample FN-1P5). Because a smaller lattice parameter ( $4.150$ - $4.152 \text{ \AA}$ ) is also seen for undoped  $\text{LiFeO}_2$  synthesized under air (ANL-84-38, p. 9), it is not known whether the nickel was successfully incorporated into  $\text{LiFeO}_2$  in this case. Samples have been sent for chemical analysis.

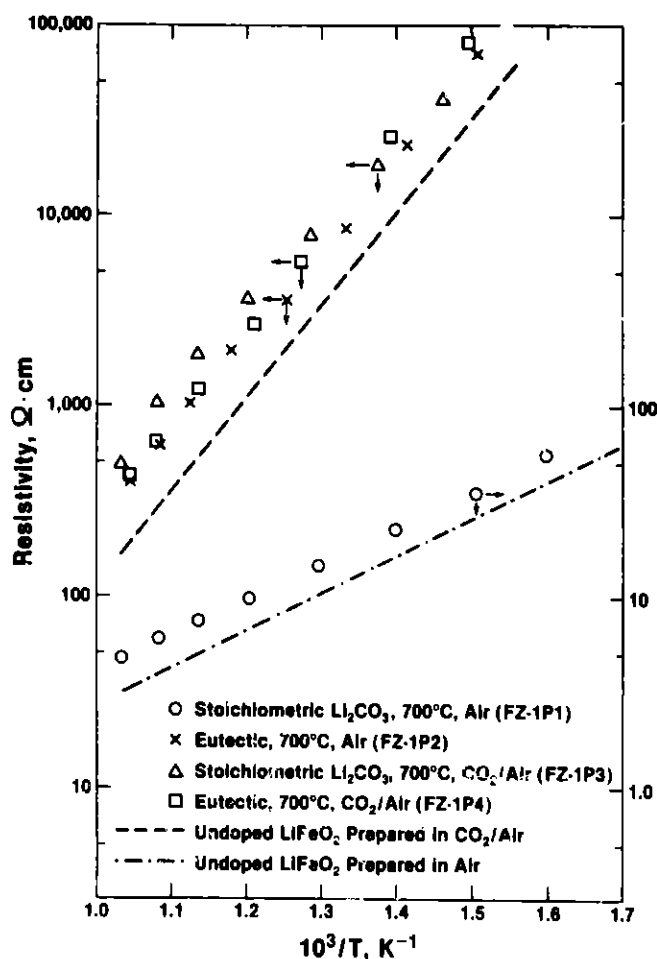


Fig. 8.

Resistivity of Zr-Doped  
 $\text{LiFeO}_2$

Table 4. Properties of Ni-Doped  $\text{LiFeO}_2$  Prepared by Coprecipitation

Sample No.	Carbonate Treatment			XRD before Sintering
	Carbonate	Temp.	Gas	
FN-1P1	Stoichiometric $\text{Li}_2\text{CO}_3$	700°C	Air	$\text{LiFeO}_2$ $a = 4.150 \text{ \AA}$
FN-1P2	$\text{Li}_2\text{CO}_3\text{-K}_2\text{CO}_3$ eutectic	700°C	Air	Broken crucible: sample lost
FN-1P4	Stoichiometric $\text{Li}_2\text{CO}_3$	700°C	30% $\text{CO}_2/\text{air}$	$\text{LiFeO}_2$ $a = 4.158 \text{ \AA}$
FN-1P5	$\text{Li}_2\text{CO}_3\text{-K}_2\text{CO}_3$ eutectic	700°C	30% $\text{CO}_2/\text{air}$	$\text{LiFeO}_2$ $a = 4.158 \text{ \AA}$ + very minor $\text{LiFe}_5\text{O}_8$

The electronic resistivity of the Ni-doped samples was measured and the data are given in Fig. 9. The sample prepared under air had much lower resistivity than the samples prepared under CO<sub>2</sub>-air, a trend also observed for undoped LiFeO<sub>2</sub> and Mn-doped LiFeO<sub>2</sub>. Doped LiFeO<sub>2</sub> materials prepared under CO<sub>2</sub>-air have resistivities comparable to those of undoped LiFeO<sub>2</sub> synthesized under similar conditions.

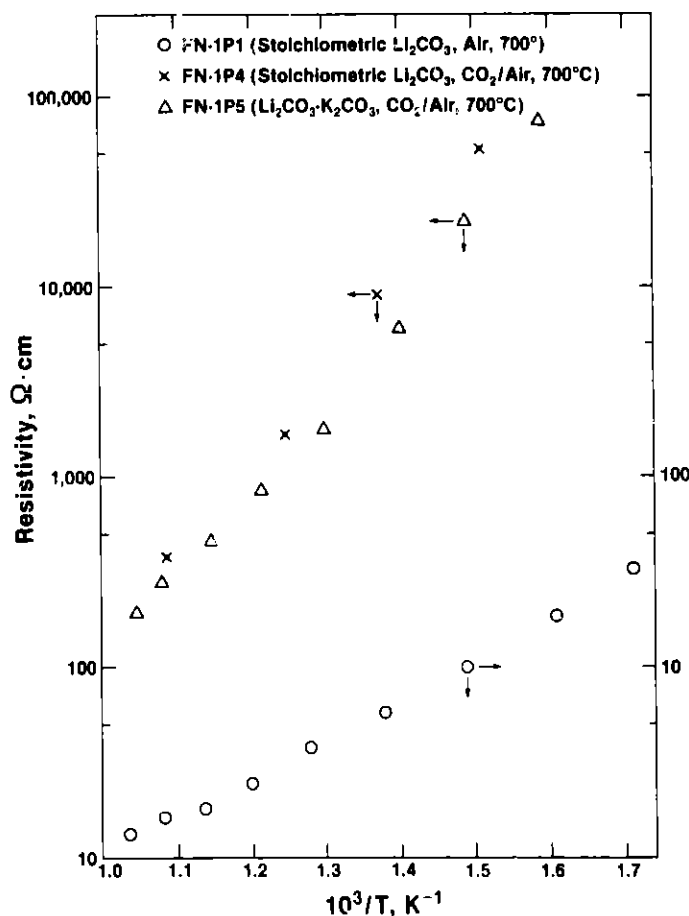


Fig. 9. Resistivity of Ni-Doped LiFeO<sub>2</sub>

The coprecipitation method was used to synthesize LiFeO<sub>2</sub> doped with copper (nominal Fe/Cu = 10/1). Lithium hydroxide solution was employed to precipitate copper and iron from nitrate solution, and the carbonate treatment was carried out at 700°C under air or CO<sub>2</sub>-air (Table 5).

Resistivity results are shown in Fig. 10 for the two Cu-doped samples prepared in air. The resistivity of the samples prepared under CO<sub>2</sub>-air has not yet been measured. It will be interesting to see how the resistivity of these samples compares with that of the samples prepared under air.

As mentioned earlier in the report, preparation temperature has an effect on the resistivity of undoped and doped LiFeO<sub>2</sub>. The previous quarterly included a preliminary thermodynamic analysis on the reaction between

Table 5. Properties of Cu-Doped  $\text{LiFeO}_2$  Samples

Sample No.	Carbonate Treatment			XRD before Sintering
	Carbonate	Temp.	Gas	
FN-1P1	Stoichiometric $\text{Li}_2\text{CO}_3$	700°C	Air	$\text{LiFeO}_2$ $a = 4.152 \text{ \AA}$ + very minor $\text{CuO}$
FN-1P2	$\text{Li}_2\text{CO}_3\text{-K}_2\text{CO}_3$	700°C	Air	$\text{LiFeO}_2$ $a = 4.156 \text{ \AA}$
FN-1P3	Stoichiometric $\text{Li}_2\text{CO}_3$	700°C	30% $\text{CO}_2/\text{air}$	TBD <sup>a</sup>
FN-1P4	$\text{Li}_2\text{CO}_3\text{-K}_2\text{CO}_3$	700°C	30% $\text{CO}_2/\text{air}$	TBD <sup>a</sup>

<sup>a</sup>TBD = to be determined.

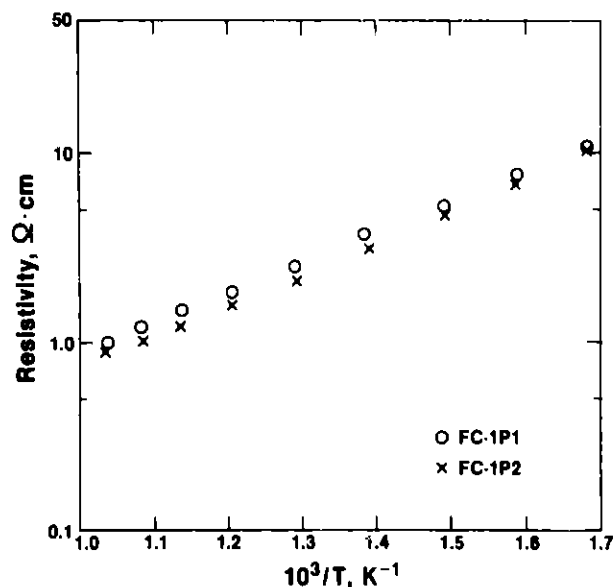


Fig. 10.

Resistivity of Cu-Doped  $\text{LiFeO}_2$

$\text{Li}_2\text{CO}_3$  and  $\text{Fe}_2\text{O}_3$  under various conditions (ANL-84-38, p. 13). In this analysis, the calculated  $\text{Fe}_2\text{O}_3$  content was found to increase with resistivity. Also, the analysis indicated that  $\text{Fe}_2\text{O}_3$  content decreases with increasing temperature. The resistivity of undoped  $\text{LiFeO}_2$  was measured at 700 and 850°C (ANL-84-38, p. 9). To determine the resistivity of  $\text{LiFeO}_2$  at a lower temperature, samples of undoped  $\text{LiFeO}_2$  were prepared at 600°C. Table 6 shows the preparation conditions and the X-ray diffraction results.

From Table 6, it can be seen that the preparation at 600°C results in  $\text{LiFeO}_2$  material with both  $\alpha$  and  $\gamma$  phases. The resistivity of three pellets of undoped  $\text{LiFeO}_2$  material synthesized at 600°C and sintered at 1050°C under air is shown in Fig. 11. The resistivity of these pellets is much higher than that of pellets prepared under air at 700°C and very similar to pellets prepared under  $\text{CO}_2$ -air at 700 and 850°C.

Table 6. Properties of Undoped  $\text{LiFeO}_2$  Prepared at  $600^\circ\text{C}$ 

Sample No.	Carbonate Treatment			XRD before Sintering
	Carbonate	Temp.	Gas	
F-22	Stoichiometric $\text{Li}_2\text{CO}_3$	$600^\circ\text{C}$	Air	$\alpha\text{-LiFeO}_2$ (4.158 Å) + $\gamma\text{-LiFeO}_2$
F-23	Excess $\text{Li}_2\text{CO}_3$	$600^\circ\text{C}$	Air	$\alpha\text{-LiFeO}_2$ (4.158 Å) + $\gamma\text{-LiFeO}_2$
F-24	$\text{Li}_2\text{CO}_3\text{-K}_2\text{CO}_3$ eutectic	$600^\circ\text{C}$	Air	$\alpha\text{-LiFeO}_2$ (4.158 Å) + $\gamma\text{-LiFeO}_2$

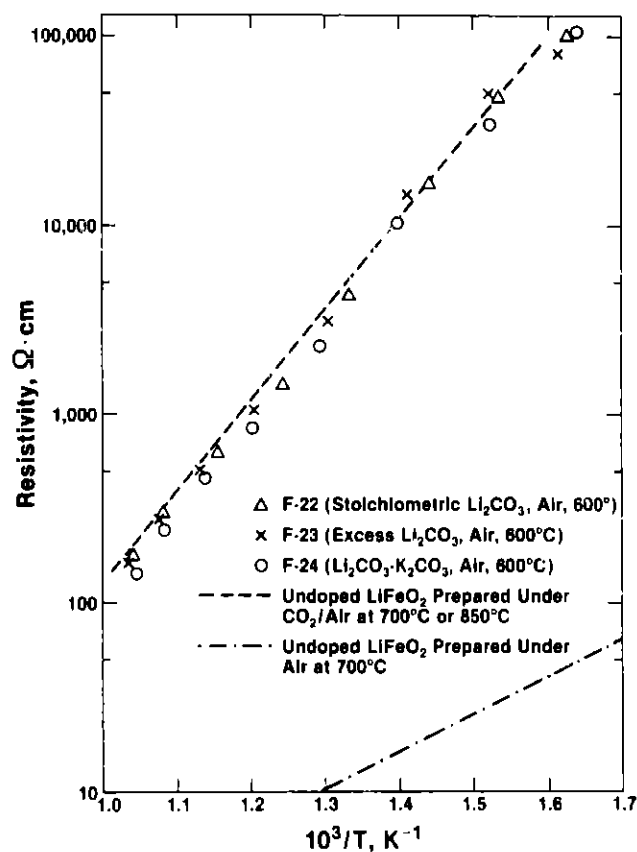


Fig. 11.

Resistivity of Undoped  $\text{LiFeO}_2$   
Prepared at  $600^\circ\text{C}$

Several undoped  $\text{LiFeO}_2$  samples were also prepared at  $700^\circ\text{C}$  under different gas atmospheres. The details for the preparation of these samples are given in Table 7. The measured electronic resistivity of the samples is shown in Figs. 12 and 13. The resistivity of undoped  $\text{LiFeO}_2$  prepared under 30%  $\text{CO}_2$ -balance air is also shown in the figures for comparison. From the results obtained so far, the resistivity of undoped  $\text{LiFeO}_2$  appears to be insensitive to the change of the oxygen content in the atmosphere in the material preparation step.

Table 7. Properties of Undoped  $\text{LiFeO}_2$  Prepared under Different Gas Atmospheres

Sample No.	Carbonate Treatment			XRD before Sintering
	Carbonate	Temp.	Gas	
F-26	Stoichiometric $\text{Li}_2\text{CO}_3$	700°C	2/3 $\text{CO}_2$ -1/3 $\text{O}_2$	$\text{LiFeO}_2$ $a = 4.158 \text{ \AA}$ + very minor $\text{LiFe}_5\text{O}_8$
F-27	$\text{Li}_2\text{CO}_3$ - $\text{K}_2\text{CO}_3$	700°C	2/3 $\text{CO}_2$ -1/3 $\text{O}_2$	$\text{LiFeO}_2$ $a = 4.158 \text{ \AA}$ + very minor $\text{LiFe}_5\text{O}_8$
F-28	Stoichiometric $\text{Li}_2\text{CO}_3$	700°C	30% $\text{CO}_2$ - $\text{O}_2$	TBD <sup>a</sup>
F-29	Excess $\text{Li}_2\text{CO}_3$	700°C	30% $\text{CO}_2$ - $\text{O}_2$	TBD <sup>a</sup>
F-30	$\text{Li}_2\text{CO}_3$ - $\text{K}_2\text{CO}_3$	700°C	30% $\text{CO}_2$ - $\text{O}_2$	TBD <sup>a</sup>

<sup>a</sup>TBD = to be determined.

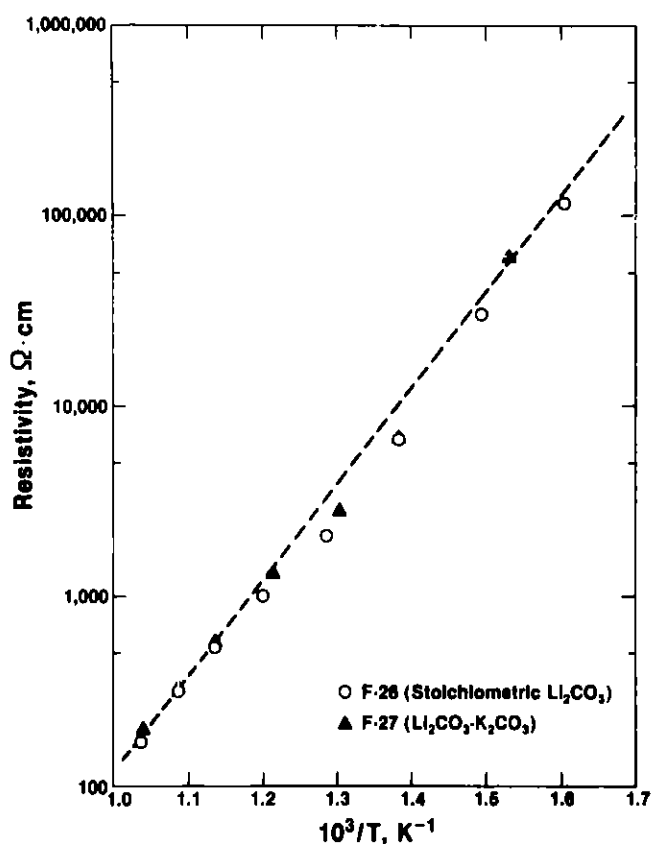


Fig. 12.

Resistivity of Undoped  $\text{LiFeO}_2$  Prepared under 2/3  $\text{CO}_2$ -1/3  $\text{O}_2$

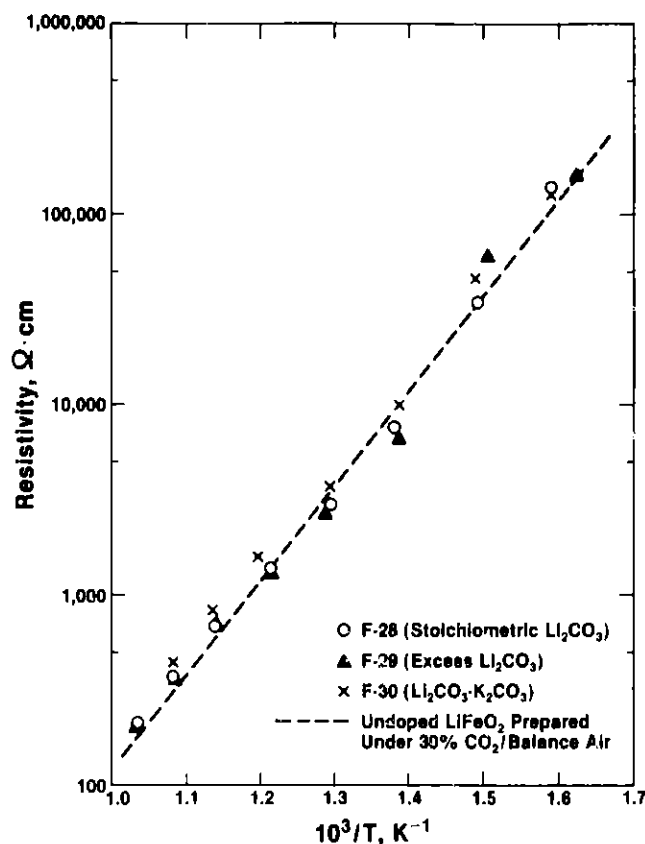


Fig. 13.

Resistivity of Undoped  
LiFeO<sub>2</sub> Prepared under  
30% CO<sub>2</sub>-70% O<sub>2</sub>

## B. Solubility of Alternative Cathode Materials (T. D. Kaun, B. A. Baumert\*)

Solubility of NiO and alternative cathode materials (Li<sub>2</sub>MnO<sub>3</sub>, LiFeO<sub>2</sub>, ZnO) is being examined for temperature dependence and effects of humidity and electrolyte compositions. Low solubility is desirable for an electrode microstructure to resist coarsening. Preparations are being made to examine solubility and electrode microstructure change ("ripening") at 10 atm of humidified cathode gas. Solubilities of dopants for the alternative cathode materials are also being examined. Alternative cathode materials are expected to require doping to impart sufficient conductivity for use in molten carbonate fuel cells. Leaching of dopant could lead to degradation of cell performance due to altered material conductivity.

### 1. NiO

The solubilities of the alternative cathode materials and NiO are presented in Fig. 14. These solubilities were determined for cathodes with 70 mol % Li<sub>2</sub>CO<sub>3</sub>-K<sub>2</sub>CO<sub>3</sub> electrolyte and humidified (20% H<sub>2</sub>O) 1/3 O<sub>2</sub>-2/3 CO<sub>2</sub> cathode gas. In the temperature range of 550-750°C (823-1023 K), only Li<sub>2</sub>MnO<sub>3</sub> had a clearly lower solubility than NiO. The results for NiO solubility at these conditions indicated a level of about 10 ppmW nickel in the carbonate. The NiO solubility slightly decreased with temperature, 11 ppmW nickel at

\* Student Research Participant from Indiana University of Pennsylvania.

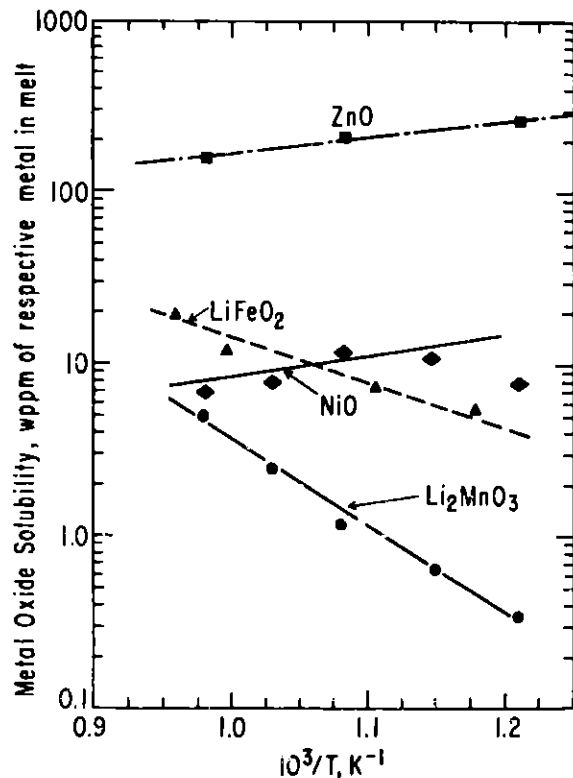


Fig. 14.

Solubilities of NiO and Alternative Cathode Materials as a Function of Temperature  
 [70 mol %  $\text{Li}_2\text{CO}_3$ -30 mol %  $\text{K}_2\text{CO}_3$ ; Humid (20%  $\text{H}_2\text{O}$ )  
 $1/3 \text{ O}_2$ - $2/3 \text{ CO}_2$  Gas]

600°C to 7 ppmW at 750°C. Earlier examination of NiO solubility in 62 mol %  $\text{Li}_2\text{CO}_3$ -38 mol %  $\text{K}_2\text{CO}_3$  and dry cathode gas indicated a solubility of about 7 ppmW nickel at 650°C. The effect of humidity upon solubility in the 70 mol %  $\text{Li}_2\text{CO}_3$ -30 mol %  $\text{K}_2\text{CO}_3$  electrolyte is not as substantial as observed earlier with 62 mol %  $\text{Li}_2\text{CO}_3$ .

Whereas earlier tests used oxidized nickel electrode material, the current NiO solubility tests used a sintered pellet formed from  $\text{Ni}(\text{OH})_2$ . Results of thermal gravimetric analysis were within 1% of the expected weight change of  $\text{Ni}(\text{OH})_2$  to NiO at 900°C. Since interest in NiO for 1-atm operation remains, these relatively low solubility levels in 70 mol %  $\text{Li}_2\text{CO}_3$  electrolyte under the humidified, enriched cathode gas are encouraging.

## 2. Zirconium-Doped ZnO and $\text{ZrO}_2$

The solubility of zinc from zirconium-doped ZnO is presented in Fig. 15. The experimental procedures for obtaining cyclic voltammograms and physical samples for analysis were identical to those described in an earlier report (ANL-83-89, pp. 16-17). For all cathode conditions, the zirconium levels were reported to be <3 ppmW in the carbonates. In the 70 mol %  $\text{Li}_2\text{CO}_3$ - $\text{K}_2\text{CO}_3$  and dry  $1/3 \text{ O}_2$ - $2/3 \text{ CO}_2$  gas conditions, the mean zinc level of 110 ppmW was somewhat lower than the 140 ppmW measured with undoped ZnO. With humidified (20%  $\text{H}_2\text{O}$ ) gas, the mean zinc level increased almost threefold, to 300 ppmW; in comparison, the undoped ZnO solubility increased by 50% due to humidity. Thus, the zirconium dopant appeared to affect the solubility of ZnO. The electrolyte composition also affected the solubility of zirconium-doped ZnO: from a mean zinc level of 200 ppmW in 62 mol %  $\text{Li}_2\text{CO}_3$  electrolyte and humid gas to 300 ppmW in 70 mol %  $\text{Li}_2\text{CO}_3$  electrolyte and humid gas.



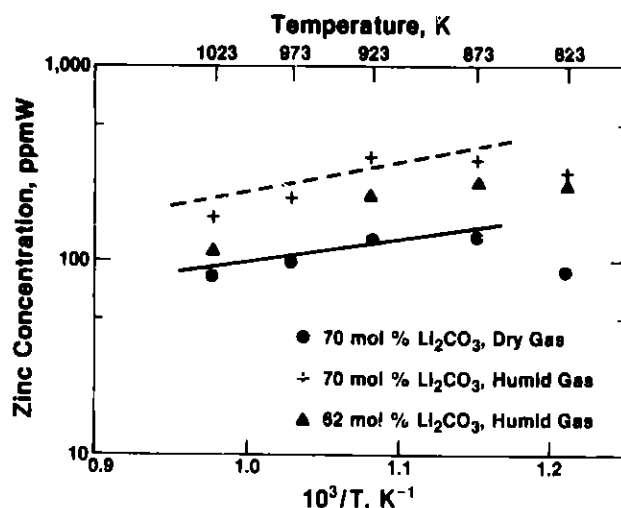


Fig. 15.

Zinc Concentration Levels due to Dissolution of Zirconium-Doped ZnO as a Function of Temperature [Humid (20% H<sub>2</sub>O) or Dry 1/3 O<sub>2</sub>-2/3 CO<sub>2</sub>, 62 or 70 mol % Li<sub>2</sub>CO<sub>3</sub>-K<sub>2</sub>CO<sub>3</sub>]

A complete examination of the solubility data revealed that zirconium levels were below the limit of detection (<1 ppmW Zr), in 62 and 70 mol % Li<sub>2</sub>CO<sub>3</sub>-K<sub>2</sub>CO<sub>3</sub> electrolyte with both dry and humid 1/3 O<sub>2</sub>-2/3 CO<sub>2</sub> cathode gas. Because of its very low solubility, zirconium is an attractive dopant.

### 3. Magnesium-Doped Li<sub>2</sub>MnO<sub>3</sub>

Our earlier solubility tests (ANL-84-38, p. 22) of magnesium-doped Li<sub>2</sub>MnO<sub>3</sub> under cathode conditions revealed rather high magnesium levels (600-900 ppmW) at 550-750°C. These results were not significantly different from those for the solubility of MgO. It has been suggested that the magnesium levels identified for the magnesium-doped Li<sub>2</sub>MnO<sub>3</sub> may be due to unincorporated MgO dopant.

To gain insight into the completeness of dopant incorporation, a sample of magnesium-doped Li<sub>2</sub>MnO<sub>3</sub> with a Mg/Mn ratio of 1/10 (synthesized by J. L. Smith, CMT) was treated in a carbonic acid wash. The weak acid was intended to dissolve the unincorporated MgO dopant. (This technique was developed earlier for preparation of ZnO solubility samples.) Deionized water (500 cm<sup>3</sup>) containing 7.5 g Li<sub>2</sub>MnO<sub>3</sub> was vigorously stirred with bubbling CO<sub>2</sub> for 24 h at room temperature. The wash solution was analyzed\* for lithium and magnesium. The washing procedure dissolved approximately 70% of the magnesium and 1% of the lithium present.

The resultant material (3 at. % magnesium dopant) is being prepared for conductivity tests, along with untreated samples prepared with 5, 10, and 15 at. % magnesium dopant. If the magnesium-doped Li<sub>2</sub>MnO<sub>3</sub> material washed with carbonic acid has comparable conductivity, we will have good evidence of incomplete incorporation of magnesium dopant. Solubility testing will be conducted on the carbonic-acid-treated material after completion of the conductivity testing.

\* E. A. Huff and A. M. Essling, ANL Analytical Chemical Laboratory.

#### 4. LiFeO<sub>2</sub>

Previous data on LiFeO<sub>2</sub> solubility were obtained with zinc-doped LiFeO<sub>2</sub>. The solubility of undoped LiFeO<sub>2</sub> under various cathode conditions, presented as a function of temperature in Fig. 16, shows an increase with an increase in temperature. For example, the LiFeO<sub>2</sub> solubility under humidified 1/3 O<sub>2</sub>-2/3 CO<sub>2</sub> gas in 70 mol % Li<sub>2</sub>CO<sub>3</sub>-K<sub>2</sub>CO<sub>3</sub> increases from 6 ppmW iron at 600°C to 12 ppmW at 750°C, with a mean value of 10 ppmW. A change of electrolyte composition (62 mol % Li<sub>2</sub>CO<sub>3</sub>) reduces LiFeO<sub>2</sub> solubility to a mean value of 6 ppmW iron. The levels of iron for LiFeO<sub>2</sub> solubility under dry gas in 62 mol % Li<sub>2</sub>CO<sub>3</sub> have a mean value of 4 ppmW. The dry-gas solubility levels range from 2 to 5 ppmW and are similar to the values determined in the earlier tests with zinc-doped LiFeO<sub>2</sub>. An increase in LiFeO<sub>2</sub> solubility was observed when the gas was humidified (about a 50% increase with 20% H<sub>2</sub>O for undoped LiFeO<sub>2</sub>).

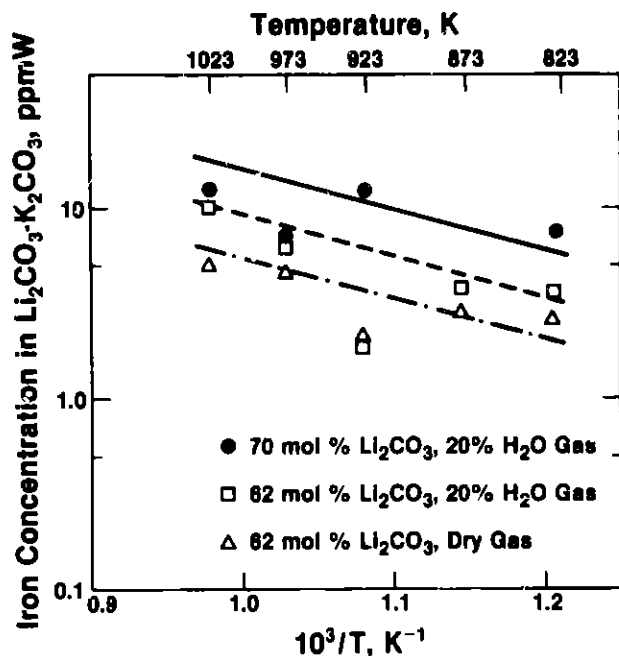


Fig. 16.

Iron Levels due to Solubility of LiFeO<sub>2</sub> as a Function of Temperature [Humid (20% H<sub>2</sub>O) or Dry 1/3 O<sub>2</sub>-2/3 CO<sub>2</sub> Gas, 62 or 70 mol % Li<sub>2</sub>CO<sub>3</sub>-K<sub>2</sub>CO<sub>3</sub>]

#### C. Effect of Gas Pressure upon Cathode Material Solubility

The objective of this effort is to determine equilibrium solubility levels of cathode material at a cathode gas pressure of 10 atm. To this end, a layer of cathode material in contact with carbonate-wetted LiAlO<sub>2</sub> layers will be held at steady-state conditions to attain equilibrium levels of solubility products in the carbonate phase. As initially proposed by J. L. Smith (CMT), a sintered LiAlO<sub>2</sub> layer wetted with carbonates would be later removed and analyzed. A number of practical limitations lead to assembly of sandwiches of tape-cast layers. Since this experimental approach depends upon diffusion of solubility products into the carbonate-wetted LiAlO<sub>2</sub> layers, contact between layers is crucial. Therefore, cathode material layers and LiAlO<sub>2</sub> layers are bonded together. After each experimental run, we plan

to remove the cathode material by abrasion and submit the remainder for chemical analysis. The initial experiment will examine solubility at 1 atm, to be compared later with 10 atm tests. Separate samples are also tested for electrode microstructure changes.

Five different "sandwiches" of tapes are on test at a cathode gas pressure of 1 atm. As seen in Fig. 17, they include three layers of  $\text{LiAlO}_2$  tape ( $1.5 \times 1$  in.), which were laminated together by brushing ethylene dichloride onto both adjoining sides and later allowing them to dry; the cathode materials ( $\text{NiO}$ ,  $\text{LiFeO}_2$ , magnesium-doped  $\text{Li}_2\text{MnO}_3$ , and  $\text{ZnO}$ ) were then laminated to the top of the  $\text{LiAlO}_2$  layers. The amount of salt (62 mol %  $\text{Li}_2\text{CO}_3$ -38 mol %  $\text{K}_2\text{CO}_3$ ) needed to "wet" both the  $\text{LiAlO}_2$  and the cathode material was calculated to provide 35% by volume for the tape-cast materials. The proper amounts of salt were added to the respective tapes, which were then cured according to the following schedule:

1. One day is allowed for bulk of ethylene dichloride to evaporate.
2. Oven is set at  $200^\circ\text{C}$  for 2 h to expel solvent (ethylene dichloride).
3. Oven is set at  $400^\circ\text{C}$  for 2 h for binder burnout.
4. Oven is set at  $650^\circ\text{C}$  for 2 h for tape curing.
5. Tape is cooled in the oven for 1-2 h before removal to prevent cracking.

It was noted in previous experimentation that (1) too much ethylene dichloride made the tape curl, and (2) each layer had to be laminated to assure bonding of the cathode material to the  $\text{LiAlO}_2$  and good contact across all points of the layers.

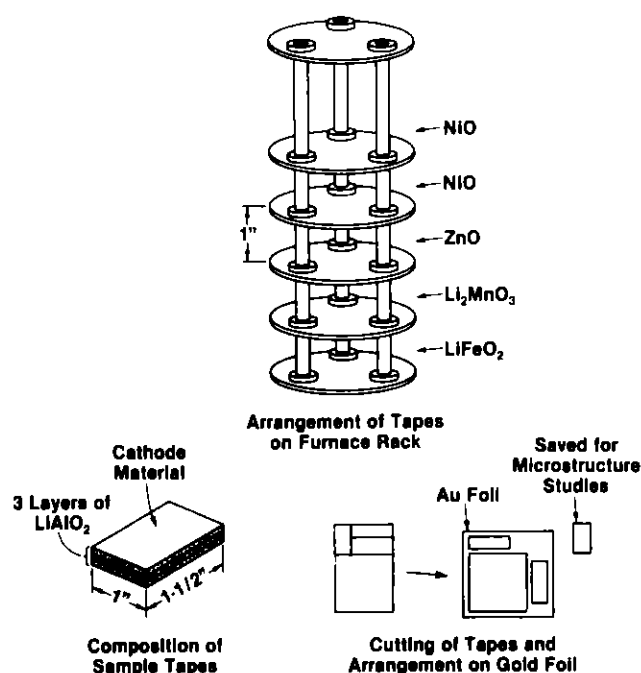
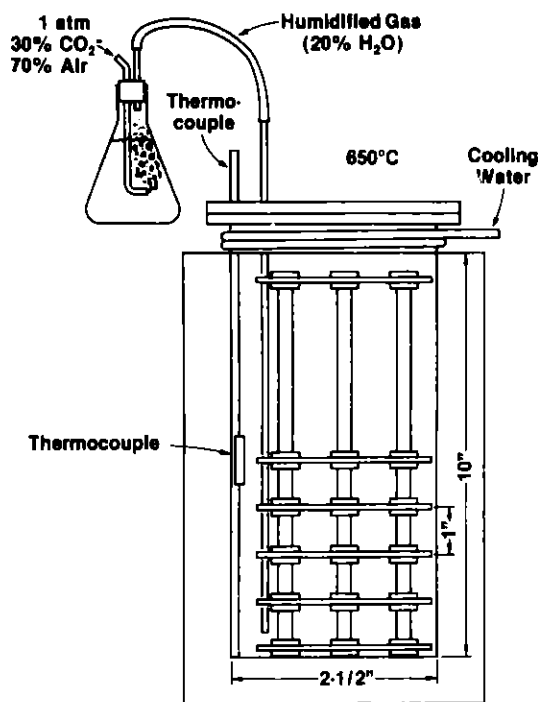


Fig. 17.

Arrangement of Samples for  
Studies of the Cathode Gas  
Pressure Effect

The prepared "sandwiches" were cut into four pieces, one of which was saved for microstructure studies. They were then placed on gold foil, which rested on the various shelves of a furnace rack, and placed in a tube furnace controlled at  $650^{\circ}\text{C}$  (see Fig. 18). The shelves were set one inch apart, as close as was convenient, to avoid any temperature gradient in the furnace. The pressure inside the furnace was one atmosphere; the gas entered the humidifier as 30%  $\text{CO}_2$ -70% air and entered the furnace with 20%  $\text{H}_2\text{O}$ . The samples were held at these conditions for 300 h. Solubility was determined from analysis of carbonate-wetted (62 mol %  $\text{Li}_2\text{CO}_3$ - $\text{K}_2\text{CO}_3$ )  $\text{LiAlO}_2$  layers after a surface layer of the cathode material was abraded away.



Furnace Setup with Rack

Fig. 18.

Solubility Apparatus for Examining  
Cathode Gas Pressure Effects at  
1 atm

The samples were prepared for analysis by first dissolving the carbonates in weak acid (in  $\text{HCl}$  or carbonic) and filtering. This solution was analyzed for solubility products contained in the carbonates. The remaining  $\text{LiAlO}_2$  was treated with concentrated  $\text{HCl}$  to leach any solubility products, which may have been incorporated with the  $\text{LiAlO}_2$ . This solution was analyzed also.

The preliminary solubility results for  $\text{NiO}$ ,  $\text{LiFeO}_2$ ,  $\text{ZnO}$ , and magnesium-doped  $\text{Li}_2\text{MnO}_3$  at 1 atm are presented below. At this point, we have not adequately determined our level of error.

Cathode Material	Solubility Result
NiO	~100 ppmW Ni in carbonate.
LiFeO <sub>2</sub>	~60 ppmW Fe in carbonate; questionable indication of Fe-doping of LiAlO <sub>2</sub> .
ZnO	~90 ppmW Zn in carbonate; 0.4 wt % Zn from LiAlO <sub>2</sub> ; apparently Zn-doping of LiAlO <sub>2</sub> .
Mg-Doped Li <sub>2</sub> MnO <sub>3</sub>	~30 ppmW Mn in carbonate; 0.33 wt % magnesium in carbonate; magnesium-doping of LiAlO <sub>2</sub> not indicated.

D. Cathode Material Migration  
(F. C. Mrazek, J. R. Stapay, J. L. Smith)

Two cells having moist cathode gases were tested for 200 h at 650°C. The cathode in one cell (11A) was magnesium-doped Li<sub>2</sub>MnO<sub>3</sub> and in the other (11B), LiFeO<sub>2</sub>. Minor construction modifications were made to reduce the contribution of the cell hardware corrosion products to the electrolyte by (1) replacing the 90% Ni-10% Cr anode structure with 100% Ni material and (2) covering the 304 stainless steel in the wet-seal zone with aluminum foil. The open circuit voltages during the test ranged from 1.07 to 1.02 V in both cells.

Macroexamination was done of many fractions through the full electrolyte thickness in both cells, which showed no evidence of the colored corrosion product layer normally present. Microscopic examination was done of polished electrolyte specimens by SEM and reflected light microscopy, which showed no large grains of nonelectrolyte cations that may have resulted from dissolution of either the anode or cathode structure or by wet-seal corrosion. Bulk chemical analyses of electrolyte from both cells are presented in Table 8. This high magnesium present in the electrolyte from Cell 11A agrees with the above solubility results (Section II.B.3).

Table 8. Electrolyte Analysis for Selected Cations

	Contaminants, <sup>a</sup> ppm				
	Fe	Cr	Mn	Ni	Mg
Unused Electrolyte	23	<3	4	<3	15
Electrolyte from Mg-doped Li <sub>2</sub> MnO <sub>3</sub> Cathode (Cell 11A)	24	115	19	8	1730
Electrolyte from LiFeO <sub>2</sub> Cathode (Cell 11B)	59	36	5	10	13

<sup>a</sup>Analytical results by E. A. Huff, ANL Analytical Chemistry Laboratory.

The measures taken to reduce the corrosion product migration into the electrolyte appear to have made our analyses of cathode-material migration more precise. Aside from the 50-75 wt % iron plus nickel and chromium, the 300-series stainless steels may contain as much as 2 wt % manganese. It is unfortunate that the magnesium dopant showed such a high solubility, but the  $\text{Li}_2\text{MnO}_3$  and  $\text{LiFeO}_2$  compounds appear to exhibit sufficient chemical stability to continue to be considered active candidates for cathode materials.

### III. COMPONENT STRUCTURE DEVELOPMENT AND EVALUATION

#### A. Cathode Structure Development

(T. D. Claar, R. J. Fousek, R. B. Poeppel)\*

The objective of this activity is the development of techniques for fabricating alternative cathode materials into thin, porous cathode structures for cell testing. The preliminary cathode specifications are a "dual porosity" structure that is approximately 0.4-mm (0.015-in.) thick and has a total porosity of 55 to 65%. Approximately half of the porosity is to consist of small pores ( $\leq 1 \mu\text{m}$ ) and the other half, larger pores ( $\sim 10 \mu\text{m}$ ).

Current cathode fabrication efforts are focusing on magnesium-doped  $\text{Li}_2\text{MnO}_3$ , which has shown low electrical resistivity ( $\sim 5 \Omega \cdot \text{cm}$  at  $650^\circ\text{C}$ ) and good chemical stability under simulated cathode conditions. During this quarter, a series of cathode tapes was prepared by tape casting of a spray-dried magnesium-doped  $\text{Li}_2\text{MnO}_3$  powder. The use of microcrystalline cellulose and corn starch as pore former additives was investigated during these tape casting experiments.

Tape casting slips were prepared by vibratory milling of the spray-dried powder (Batch LMM-2) in an acrylic-based binder system (Cladan Cerbind 73131<sup>†</sup>). The formulations of these tape casting slips are summarized in Table 9. Type Z-3 Menhaden fish oil was used as a deflocculant in each of these tests. After vibratory milling to disperse the powder, the slips were de-aired by partially evacuating to 0.5 atm and then cast onto a Teflon substrate with a moving doctor blade. All of the slips were cast without difficulty, yielding tapes with good flexibility and free of cracks or air-bubble related defects.

Tapes LIM-10 and -16 were fabricated from the magnesium-doped  $\text{Li}_2\text{MnO}_3$  powder without any pore former additions. Tape LIM-17 was fabricated with a corn starch addition to introduce macroporosity in the pore diameter range of 5 to  $10 \mu\text{m}$ . The particle size and morphology of the corn starch used in the test are shown in the scanning electron micrograph in Fig. 19a. The remaining tapes (LIM-11 through -15) were formulated to contain varying levels of a cellulosic pore former. The pore former additive used in these tests was Avicel PH-105 microcrystalline cellulose (MCC),<sup>‡</sup> which is a purified and depolymerized alpha cellulose derived from fibrous plants. It is a white, free-flowing powder which is insoluble in water and organic solvents. Burnout of MCC occurs in the temperature range of  $325\text{--}375^\circ\text{C}$ , with a low ash content of  $<40 \text{ ppmW}$  and a heavy metal content of  $<10 \text{ ppmW}$ . Microcrystalline cellulose is widely used as a macropore former addition in the manufacture of various types of supported catalysts and catalyst carriers. The Avicel PH-105 MCC powder used in the cathode tape casting experiments has a nominal average particle diameter of  $20 \mu\text{m}$ . The scanning electron micrograph of Fig. 19b reveals the particle size distribution and morphology of the Avicel PH-105 MCC powder. The particles generally have elongated shapes, an advantageous feature for incorporation of interconnected macroporosity within the cathode structure. Other grades of MCC having nominal average particle sizes of 50 and  $100 \mu\text{m}$  are also available.

---

\* Materials Science and Technology Division, ANL.

† Cladan Technology, Inc., San Marcos, CA.

‡ Trademark of FMC Corp., Philadelphia, PA.

Table 9. Summary of  $\text{Li}_2\text{MnO}_3$  Tape Casting Experiments

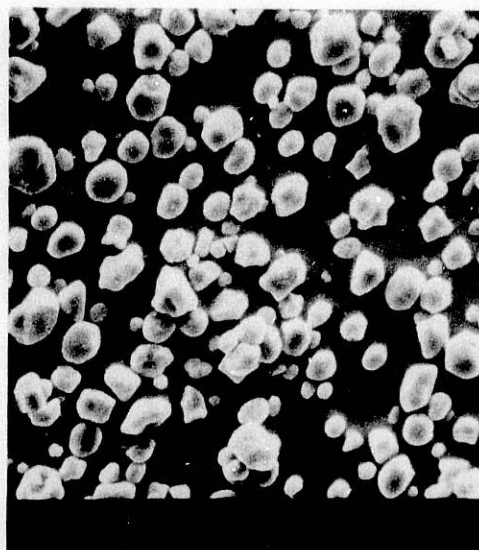
Slip No.	Composition	Tape Thickness, in.	
		As-cast	Dried
LIM-10	40 g $\text{Li}_2\text{MnO}_3$ -Mg (LMM-2) 50 g Cerbind 73131 <sup>a</sup> 0.5 g Z-3 fish oil	0.040	0.017-0.018
LIM-11	20 g $\text{Li}_2\text{MnO}_3$ -Mg (LMM-2) 50 g Cerbind 73131 0.5 g Z-3 fish oil 3.3 g Avicel PH-105 MCC <sup>b</sup>	0.040	0.014-0.015
LIM-12	20 g $\text{Li}_2\text{MnO}_3$ -Mg (LMM-2) 50 g Cerbind 73131 0.5 g Z-3 fish oil 6.7 g Avicel PH-105 MCC <sup>b</sup>	0.040	0.016-0.017
LIM-13	20 g $\text{Li}_2\text{MnO}_3$ -Mg (LMM-2) 50 g Cerbind 73131 0.5 g Z-3 fish oil 10 g Avicel PH-105 MCC <sup>b</sup>	0.040	0.016-0.018
LIM-14	30 g $\text{Li}_2\text{MnO}_3$ -Mg (LMM-2) 50 g Cerbind 73131 0.5 g Z-3 fish oil 5 g Avicel PH-105 MCC <sup>b</sup>	0.040	0.015-0.016
LIM-15	40 g $\text{Li}_2\text{MnO}_3$ -Mg (LMM-2) 50 g Cerbind 73131 0.5 g Z-3 fish oil 6.6 g Avicel PH-105 MCC <sup>b</sup>	0.040	0.014-0.015
LIM-16	30 g $\text{Li}_2\text{MnO}_3$ -Mg (LMM-2) 50 g Cerbind 73131 0.5 g Z-3 fish oil	0.040	0.013-0.014
LIM-17	30 g $\text{Li}_2\text{MnO}_3$ -Mg (LMM-2) 50 g Cerbind 73131 0.5 g Z-3 fish oil 5 g corn starch	0.040	0.016-0.017

<sup>a</sup>Cladan Technology, Inc., San Marcos, CA.<sup>b</sup>FMC Corp., Philadelphia, PA.





(A) MICROCRYSTALLINE CELLULOSE  
(FMC AVICEL PH-105)



(B) CORN STARCH

Fig. 19. Scanning Electron Micrographs of Organic Pore Formers Used in Tape Cast  $\text{Li}_2\text{MnO}_3$ -Mg Cathodes

Disk-shaped specimens of one-inch diameter were punched from each tape, placed on alumina setter plates, and heat treated for organic burnout and sintering studies. The firing schedule consisted of heating slowly from room temperature to  $400^\circ\text{C}$  over a period of 10 h for organic burnout, followed by heating at a rate of  $50\text{--}100^\circ\text{C/h}$  to a sintering temperature of  $1200\text{--}1300^\circ\text{C}$ . Weight and dimensional measurements taken before and after firing were used to estimate the degree of porosity in the green and fired cathode tapes. Results obtained from tape specimens fired at  $1250^\circ\text{C}$  for 1 h in air are summarized in Table 10. Green tapes fabricated without any organic pore former additions contained 64% porosity. Additions of MCC resulted in increased green-tape porosities of 69 to 84%, depending on the relative amount of MCC used. Tape LIM-17, containing corn starch (0.17 weight ratio of starch to ceramic), had a green porosity of  $\sim 75\%$ . Tapes sintered 1 h at  $1250^\circ\text{C}$  without pore formers had porosities of 47 to 50%, while sintered tapes containing MCC had porosities ranging from 54 to 78%. The effect of Avicel MCC and corn starch additions on increasing the total porosity and fraction of macroporosity is shown in Fig. 20, which presents scanning electron micrographs for specimens fired at a temperature of  $1250^\circ\text{C}$  for 1 h. Mercury porosimetry measurements are being performed to determine the porosity and pore-size distributions obtained in sintered tapes without any pore formers and with corn starch and microcrystalline cellulose additions.

Although the small disk specimens had sufficient strength to be handled after sintering, most specimens were not flat enough for assembly into a fuel cell. Because of the ease of handling the flexible, unfired cathode tapes, future work will emphasize fabrication and characterization of green tapes to be assembled directly into fuel cells for testing. Using this approach, one would be able to remove the organic binder, plasticizer, and pore formers from the tape in situ during heatup of the cell.

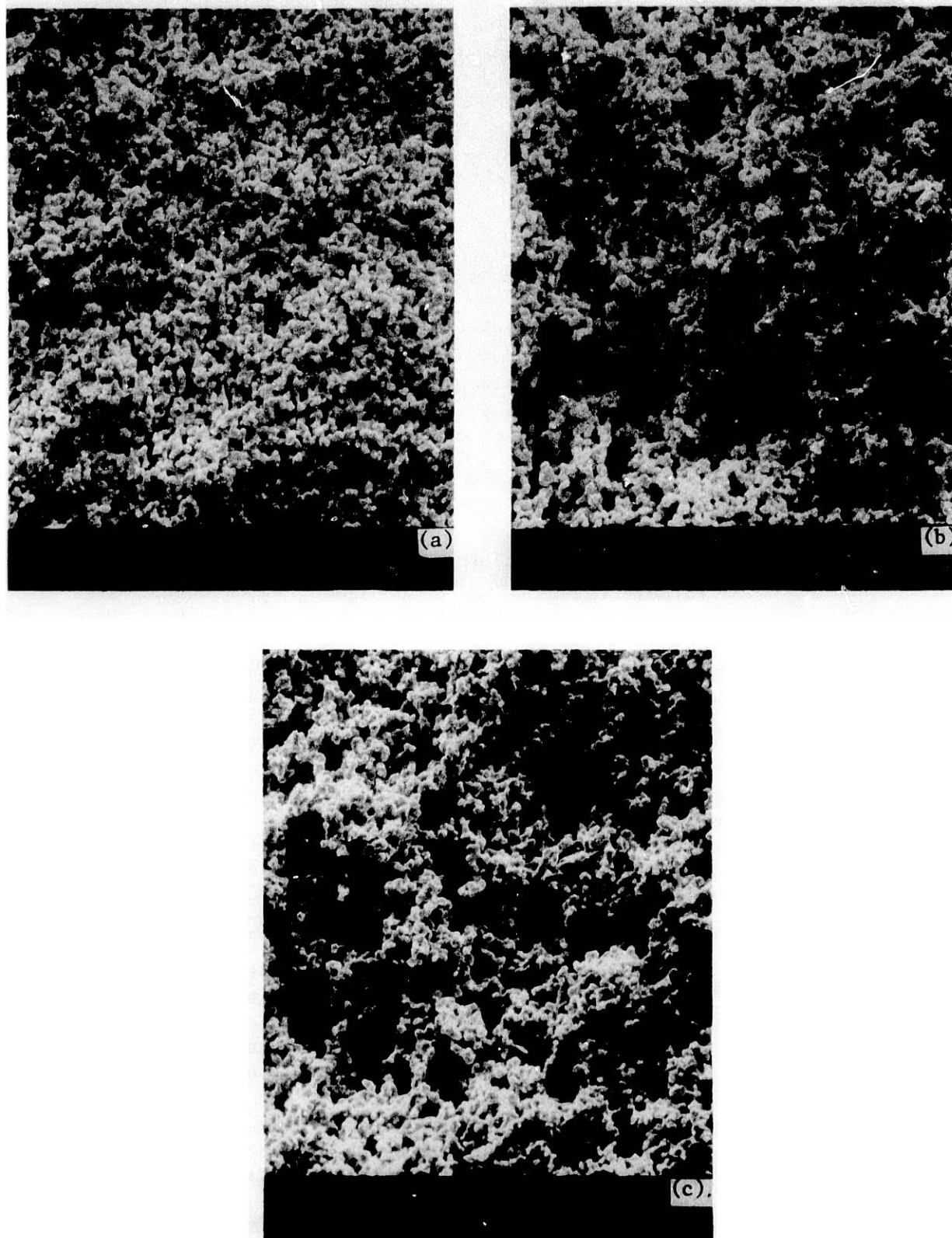


Fig. 20. Scanning Electron Micrographs of Mg-Doped  $\text{Li}_2\text{MnO}_3$  Tapes Sintered 1 h at  $1250^\circ\text{C}$  in Air: (a) No Addition (LIM-16-5); (b) Addition of Avicel PH-105 MCC Pore Former at an MCC/Ceramic Ratio of 0.17 (LIM-14-5); and (c) Addition of Corn Starch Pore Former at a Starch/Ceramic Ratio of 0.17 (LIM-17-2)

Table 10. Magnesium-Doped  $\text{Li}_2\text{MnO}_3$  Tapes Sintered  
1 h at 1250°C in Air

Tape No.	Pore Former/Ceramic Weight Ratio	Porosity in Green Tape, %	Porosity in Fired Tape, %
LIM-10	0	64.4	49.7
LIM-11	0.17 <sup>a</sup>	78.8	Specimen warped
LIM-12	0.34 <sup>a</sup>	81.7	71.6
LIM-13	0.50 <sup>a</sup>	84.4	78.1
LIM-14	0.17 <sup>a</sup>	70.8	56.1
LIM-15	0.17 <sup>a</sup>	68.8	53.5
LIM-16	0	64.0	46.7
LIM-17	0.17 <sup>b</sup>	74.6	Specimen warped

<sup>a</sup>Avicel PH-105 microcrystalline cellulose.

<sup>b</sup>Corn Starch.

#### B. Evaluation of Anode Creep Resistance

(R. B. Poeppel, T. D. Claar, R. J. Fousek, J. Emerson)\*

A new activity was initiated in January 1984. The objective of the activity is to obtain an improved understanding of anode creep and densification phenomena that occur under fuel-cell operating conditions. Both state-of-the-art and developmental anodes will be evaluated under the range of thermomechanical conditions expected in a molten carbonate fuel cell stack. A better understanding of the fundamental anode densification mechanisms is required to identify the preferred approaches for improving the anode creep resistance. An experimental technique is being developed to determine the densification behavior of porous anode structures as a function of temperature and compressive stress. The possible influence of gas composition, carbonate films, and other environmental factors will be investigated.

Contacts are being made with several industrial fuel cell contractors to obtain as-fabricated and tested anode structures. Specimens of chromium-stabilized nickel, nickel- $\text{LiAlO}_2$  cermets, nickel- or copper-plated ceramics, and other anodes supplied by various industrial contractors will be evaluated on a consistent basis. Such analytical techniques as quantitative stereology, mercury porosimetry, and scanning electron microscopy will be used to characterize porosity, pore-size distribution, and particle size of the porous anode structures. Auger electron spectroscopy, electron spectroscopy for chemical analysis (ESCA), and energy dispersive X-ray spectroscopy will be

\*Materials Science and Technology Division, ANL.

employed as appropriate to establish the chemical state and spatial distribution of chromium and other anode stabilizer additives. Experimental results will be analyzed with existing models for sintering of porous compacts to identify the dominant mechanism(s) and factors controlling anode densification. Based on these results, preferred approaches to improving the long-term structural stability of anodes will be recommended for further development.

The high-temperature test apparatus shown in Fig. 21, originally designed for studies of electrolyte creep (ANL-79-84, pp. 25-29), is being adapted to perform the anode creep measurements. The apparatus consists of a quartz tube in which the gaseous environment can be maintained, an external heater (furnace), and a load train. The load train, which was designed for relatively light loads, is being replaced with a compression cage shown in Fig. 22. The compression cage is suspended from above and the load is hung beneath. The arrangement of loading rods places the specimen in compression. This technique is suitable for the loads we expect to apply to anode samples.

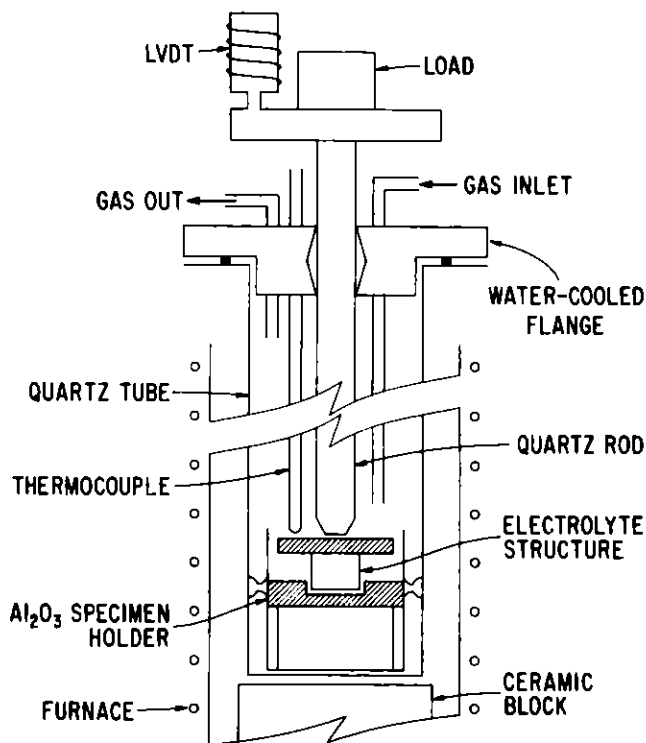


Fig. 21.

Schematic of Apparatus Used to Monitor Thermomechanical Behavior (LVDT = linear voltage/displacement transducer)

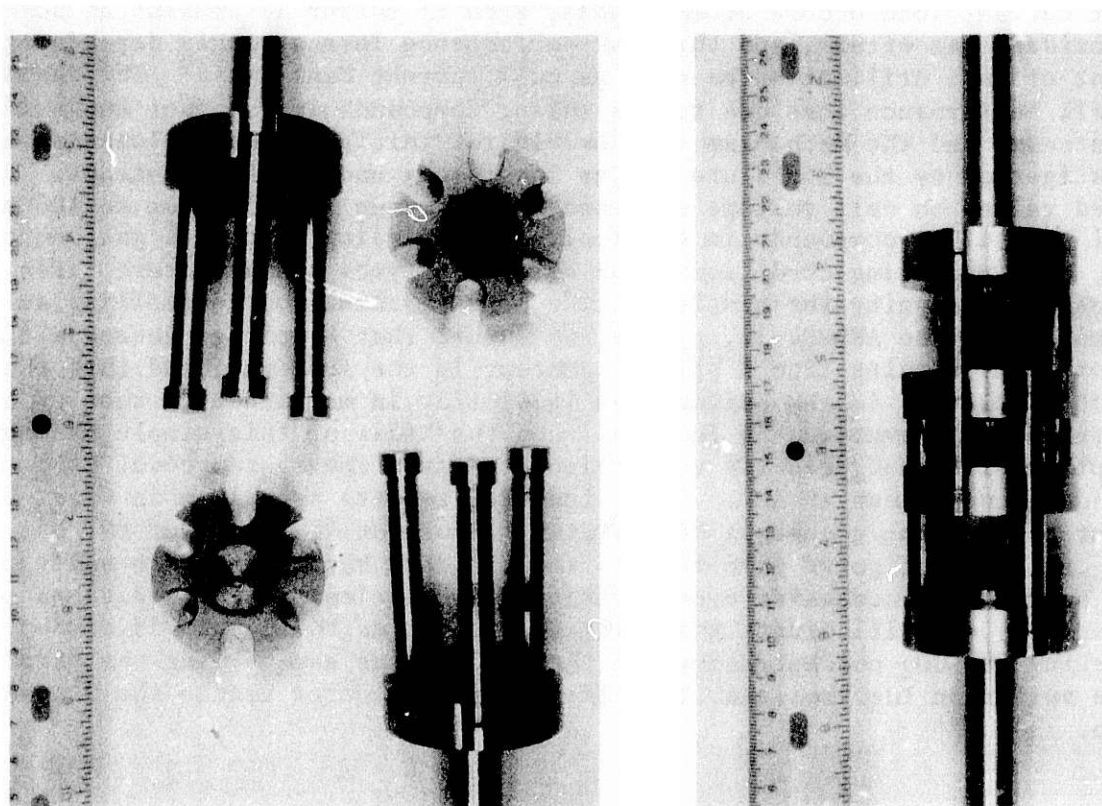


Fig. 22. Compression Cage for Anode Creep Tests Assembled (right) and Disassembled (left). The black clay represents the test specimen.

#### IV. GAS CLEANUP SYSTEM ANALYSIS (H. S. Huang, M. Krumpelt)

Sulfur species in the fuel or oxidant gas of a molten carbonate fuel cell can degrade performance. It has been stated that all performance loss under current load occurs at the anode, even if sulfur is present as  $\text{SO}_2$  in the oxidant gas stream, and that the performance loss strongly depends on the extent of fuel utilization as well as cell current density.<sup>1,2</sup> The degree of cell performance loss due to the sulfur compounds in the fuel and oxidant gas streams and the mechanism responsible for this performance loss are under investigation by the Institute of Gas Technology under a DOE contract. Reported values on cell voltage drop under load range from 5 mV up to 100 mV per 1 ppm sulfur compounds in the fuel gas, depending upon fuel gas composition, cell operating conditions, and electrode types and structure. For the purpose of analyzing the simple cathode bypass scheme for controlling sulfur accumulation (see ANL-84-38, p. 36), we assume that a voltage decrease of 10, 15, or 20 mV results from 1 ppm  $\text{H}_2\text{S}$  content in the fuel gas, and that the impact of the  $\text{SO}_2$  in the oxidant gas is similar in magnitude to that of the equivalent  $\text{H}_2\text{S}$  level in the fuel gas. On the basis of this simple assumption, the plant efficiency results were calculated from the system code, SALT, which is under development at ANL. The calculated results are given in Figs. 23 to 31 for the natural gas-based MCFC system at fuel utilizations of 80, 85, and 90%. All these figures give results for (1) zero bypass and zero sulfur, (2) zero sulfur but increasing bypass ratio, and (3) simultaneous additions of  $\text{H}_2\text{S}$  and  $\text{SO}_2$ . To illustrate the relative impacts on the plant efficiency of depleting the  $\text{CO}_2$  concentrations in the oxidant gas and varying the steady-state sulfur in the fuel gas, the efficiency is plotted versus the bleed-off ratio.

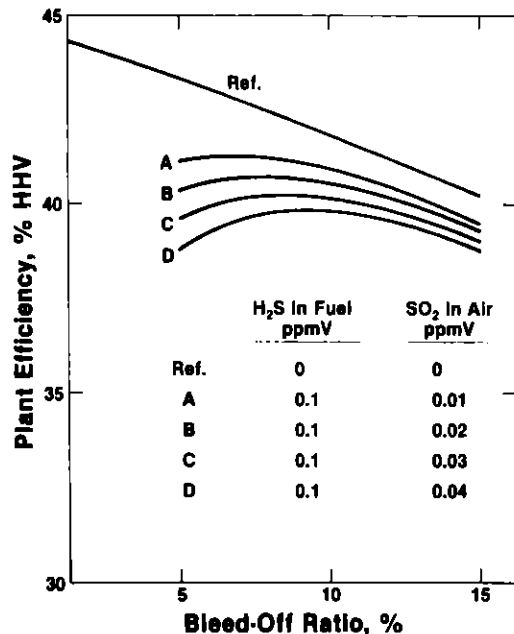


Fig. 23.

Effect of Bleed-Off and Sulfur Contents on Plant Efficiency at 80% Fuel Utilization (1 ppm eq.  $\text{H}_2\text{S}$  corresponds to 10 mV voltage drop)

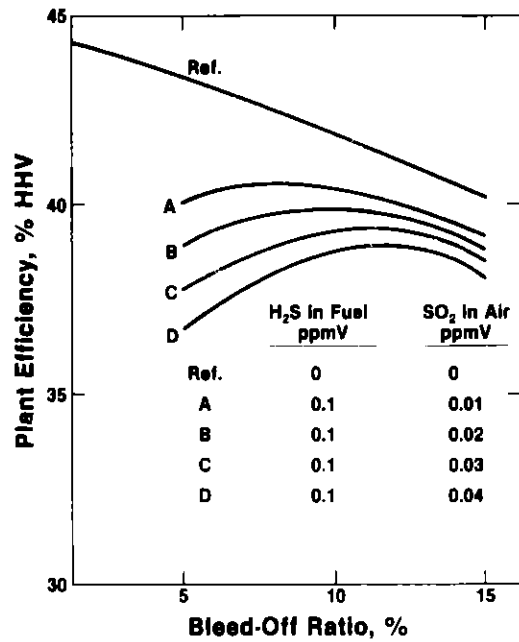


Fig. 24.

Effect of Bleed-Off and Sulfur Contents on Plant Efficiency at 80% Fuel Utilization (1 ppm eq. H<sub>2</sub>S corresponds to 15 mV voltage drop)

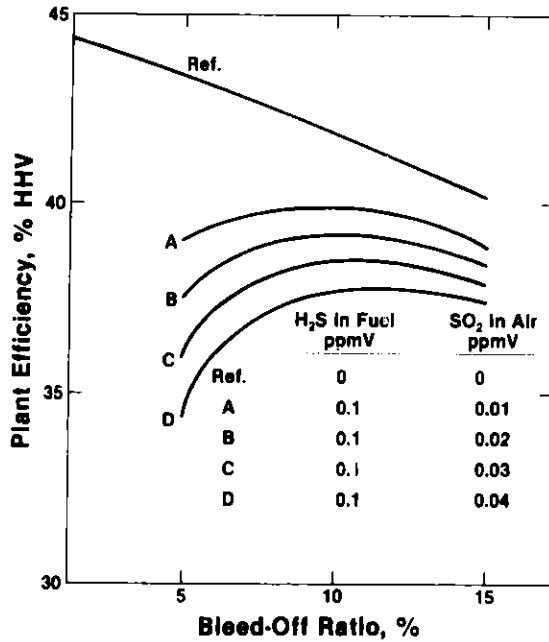


Fig. 25.

Effect of Bleed-Off and Sulfur Contents on Plant Efficiency at 80% Fuel Utilization (1 ppm eq. H<sub>2</sub>S corresponds to 20 mV voltage drop)

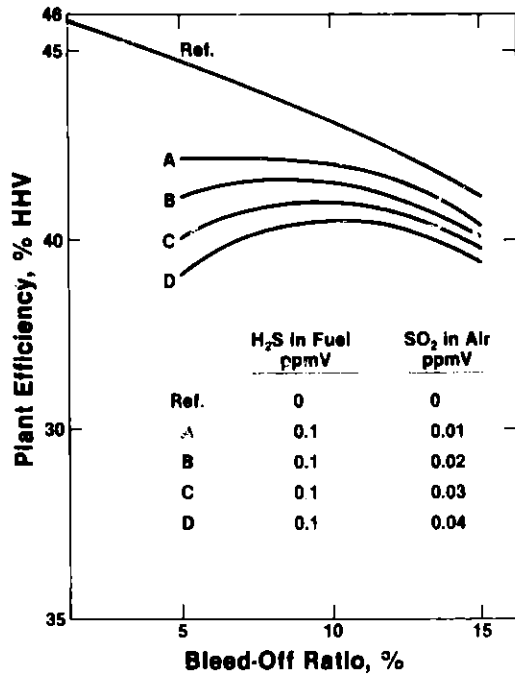


Fig. 26.

Effect of Bleed-Off and Sulfur Contents on Plant Efficiency at 85% Fuel Utilization (1 ppm eq. H<sub>2</sub>S corresponds to 10 mV voltage drop)

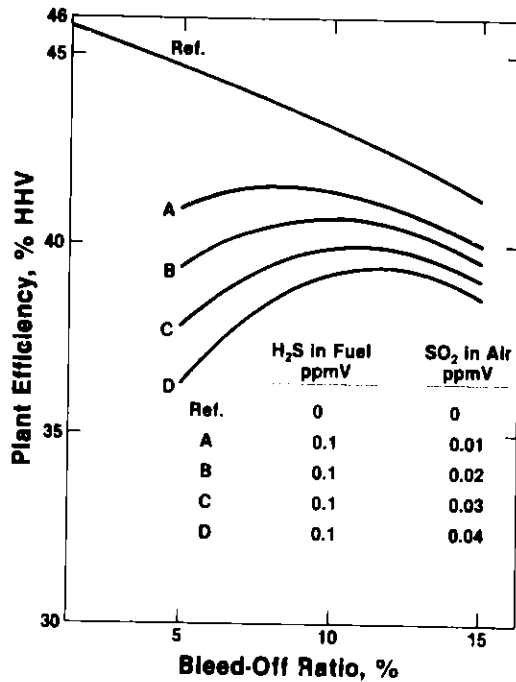


Fig. 27.

Effect of Bleed-Off and Sulfur Contents on Plant Efficiency at 85% Fuel Utilization (1 ppm eq. H<sub>2</sub>S corresponds to 15 mV voltage drop)



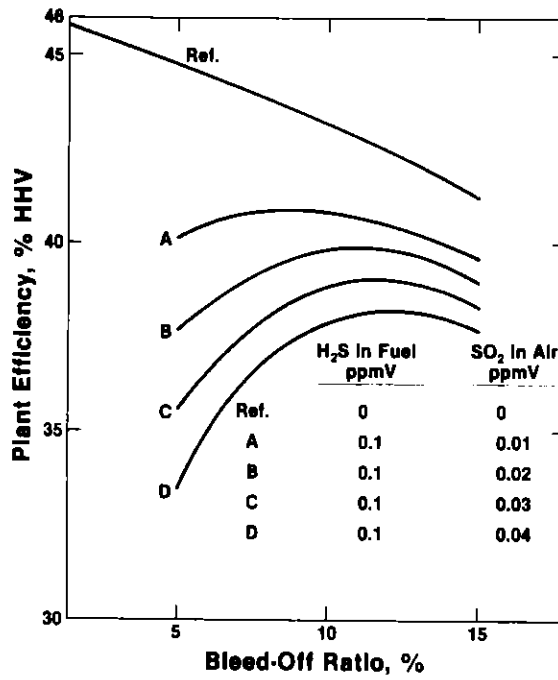


Fig. 28.

Effect of Bleed-Off and Sulfur Contents on Plant Efficiency at 85% Fuel Utilization (1 ppm eq. H<sub>2</sub>S corresponds to 20 mV voltage drop)

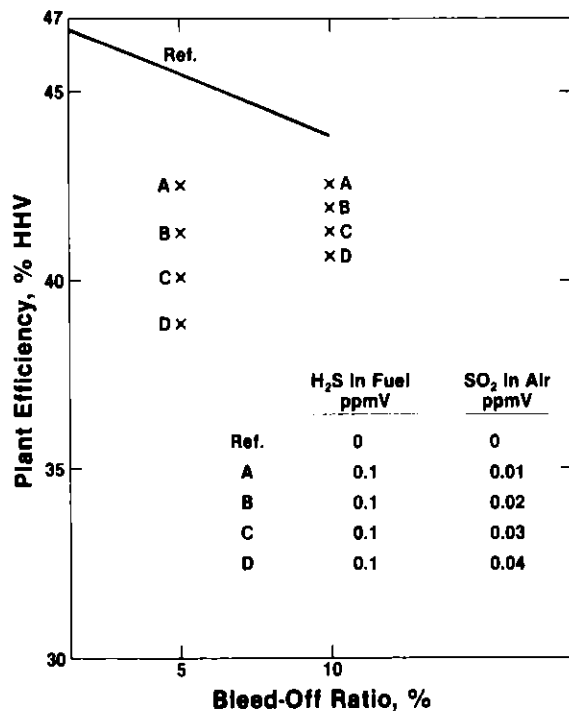


Fig. 29.

Effect of Bleed-Off and Sulfur Contents on Plant Efficiency at 90% Fuel Utilization (1 ppm eq. H<sub>2</sub>S corresponds to 10 mV voltage drop)

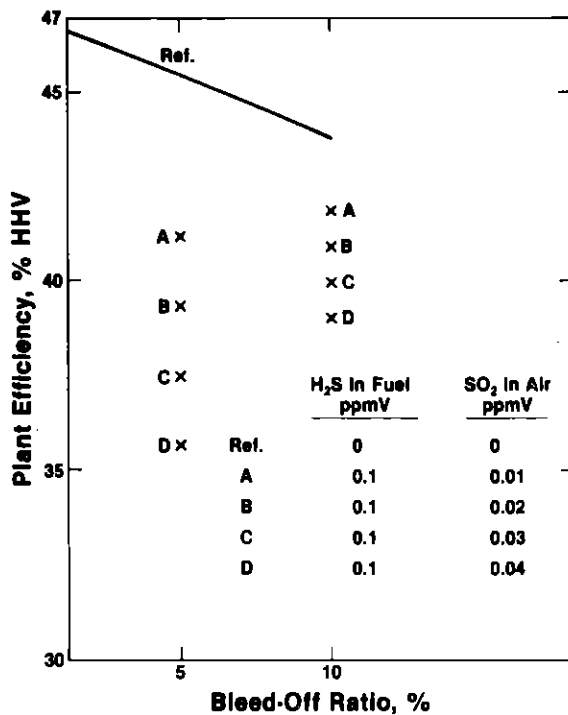


Fig. 30.

Effect of Bleed-Off and Sulfur Contents on Plant Efficiency at 90% Fuel Utilization (1 ppm eq. H<sub>2</sub>S corresponds to 15 mV voltage drop)

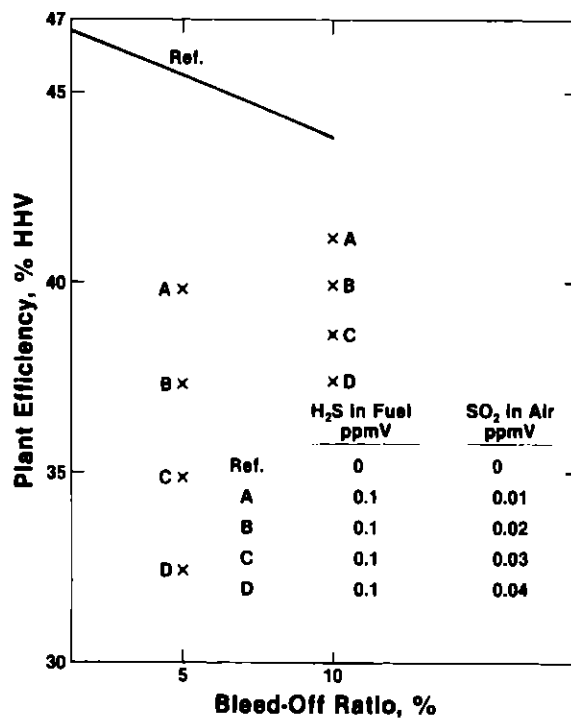


Fig. 31.

Effect of Bleed-Off and Sulfur Contents on Plant Efficiency at 90% Fuel Utilization (1 ppm eq. H<sub>2</sub>S corresponds to 20 mV voltage drop)

Figure 23 assumes 80% fuel utilization and a sulfur effect of 10 mV/ppm  $\text{H}_2\text{S}$ . For the case of zero sulfur, one notes a decrease in system efficiency ranging from 1 to 4 percentage points in bypassing the cathode with 5-15% of the gas. When sulfur is present (curves A to D), the efficiency is lowered, and the efficiency vs. bleed-off ratio curves have maxima. Curve D in Fig. 23, for instance, shows that, for 0.1 ppm  $\text{H}_2\text{S}$  in the fuel and 0.04 ppm  $\text{SO}_2$  in the air, the highest efficiency is attained at 9.5% bypass. At low bleed-off ratios, the effect of sulfur on the cell potential is more pronounced, and at high ratios depletion of  $\text{CO}_2$  has a more severe impact.

As expected, the plant-efficiency penalty increases (or the net plant efficiency decreases) with increases in the  $\text{SO}_2$  levels in the air (curves A-D). For sulfur effects of 15 and 20 mV/ppm  $\text{H}_2\text{S}$  (Figs. 24 and 25) the location of the maxima is still near 10% bypass. With the exception of two cases (curves A in Figs. 23 and 26) in which low sulfur level in air and small sulfur impact on cell voltage are assumed, the optimum (highest net plant efficiency) operation appears to be around 10% bleed-off for all the fuel utilizations considered. The optimum bleed-off increases slightly as the sulfur content in the air or the magnitude of sulfur impact on the cell voltage increases.

In Fig. 32, 10% bleed-off of the cathode inlet gas is assumed. The points with the highest net plant efficiency appear to be associated with 90% fuel utilizations under the conditions of low-to-medium sulfur contents in the air and small sulfur impact on the cell voltage. The optimal fuel utilization with respect to plant efficiency, however, gradually diminishes with increasing sulfur contents in the air and increasing magnitude of sulfur impact on the cell voltage. The optimum points eventually shift to around 85% fuel utilizations under conditions of high sulfur contents in the air and large sulfur impact on the cell voltage. It will probably be impractical to

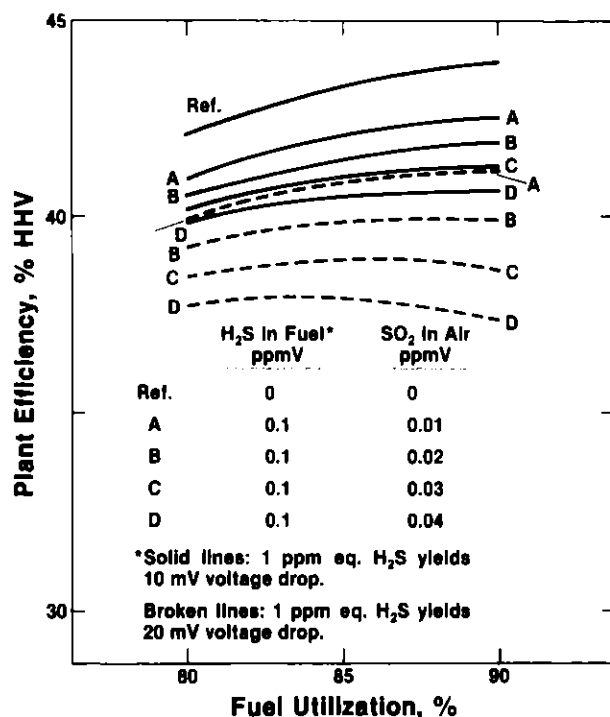


Fig. 32.

Effect of Fuel Utilization and Sulfur Contents on Plant Efficiency at 10% Bleed-Off

operate above about 85% fuel utilizations since at these utilizations the separator plates could be damaged by anodic oxidation from local fuel-flow variations; therefore, operation is likely to be about 85% fuel utilization and 10% bleed-off of cathode inlet gas.

The plant efficiency penalty arising from the application of cathode gas bleed-off as a simple means for sulfur control within a natural gas-fueled fuel cell plant is substantial even at optimum operation; it ranges from 3.5 to 8 percentage points, depending on the assumptions made. On the other hand, the savings in capital and operating cost from eliminating SO<sub>2</sub> cleanup of the air may be substantial.

The penalty on plant efficiency, however, is expected to be smaller with a coal-based fuel cell plant as opposed to a natural-gas-based one. This is so because CO<sub>2</sub> concentration in the cathode gas is higher, and less incoming air (per unit of fuel gas) is fed directly into the cathodic side of the fuel cells.

## V. MODEL DEVELOPMENT FOR SOLID OXIDE FUEL CELL

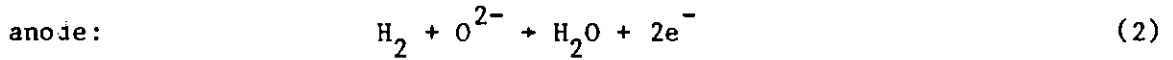
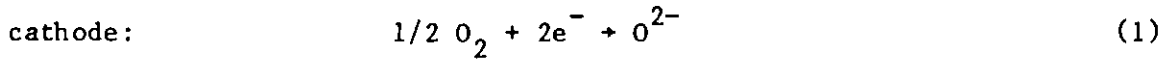
### A. Introduction (S. A. Zwick)

The goal of this work is to develop a model of solid oxide fuel cell (SOFC) performance. After verification, such a model will show the tradeoffs in cell performance arising from changes in cell design and operation. The current SOFC model incorporates the basic cell thermodynamics, cell resistance, and heat transfer processes to calculate the cell current distribution, outlet voltage, and axial temperature profile.

### B. Cell Thermodynamics

The cell thermodynamics for the SOFC model is described below.

The SOFC electrochemically reacts the hydrogen with oxygen. The reactions occurring are:



At the cathode (lanthanum manganite), oxygen accepts electrons from the external circuit to form oxygen ions. The ions are conducted through the electrolyte (zirconium dioxide) to the anode. At the anode (Co or Ni in a ZrO<sub>2</sub> matrix), hydrogen in the fuel gas reacts with the oxygen ions from the electrolyte to form water, giving up electrons to the external circuit. The overall cell reaction is



The maximum cell performance can be predicted from thermodynamic considerations, using Eq. 3. The free energy change,  $\Delta G$ , is given by

$$\begin{aligned} \Delta G = & \Delta G_f(\text{H}_2\text{O}) + RT \ln P_{\text{H}_2\text{O}} - \left[ \Delta G_f(\text{H}_2) + RT \ln P_{\text{H}_2} \right] \\ & - 1/2 \left[ \Delta G_f(\text{O}_2) + RT \ln P_{\text{O}_2} \right] \end{aligned} \quad (4)$$

where  $P$  is pressure (atm),  $R$  is the gas constant ( $8.317 \text{ J K}^{-1} \text{ mol}^{-1}$ ),  $T$  is temperature (K), and  $\Delta G_f$  is the standard free energy of formation from the elements. Because  $\Delta G_f$  is zero for hydrogen and oxygen,

$$\Delta G = \Delta G_f(\text{H}_2\text{O}) - RT \ln \frac{P_{\text{H}_2} (P_{\text{O}_2})^{1/2}}{P_{\text{H}_2\text{O}}} \quad (5)$$

The cell voltage,  $E$ , equals  $-\Delta G/nF$ , where  $n$  is the number of electrons transferred (two for Eq. 3), and  $F$  is Faraday's constant, 96,500 coulombs/equivalent. Rearranging gives the familiar Nernst equation

$$E = E^\circ + \frac{RT}{nF} \ln \frac{P_{H_2} (P_{O_2})^{1/2}}{P_{H_2O}} \quad (6)$$

where  $E^\circ = -\Delta G_f(H_2O)/nF$ .

### C. Internal Reform

Internal reform of light hydrocarbon fuels is an important feature of solid oxide fuel cells. Direct reform within the anode channel greatly simplifies the system design by eliminating the need for an external reformer. The simpler design strongly implies reduced cost and higher reliability.

Internal reform affects the temperature distribution within a SOFC generator. The reform reactions are endothermic and cool the cell. For example, the reform of methane



removes approximately 250 kJ/mol. The worst-case effect of this cooling action was calculated from the SOFC model and is shown in Fig. 33. The reform of all the methane immediately on contact with the anode surface would result in a sharply lower temperature (as much as 150 K) than that of a similar cell operating on externally reformed fuel. Consideration of two features not yet included in the model (time for the reaction to attain equilibrium and radiant heat transfer) is expected to reduce the steep temperature gradient shown in Fig. 33. The reform reaction does not immediately come to equilibrium as assumed for the figure for two reasons. First, the reaction of methane at a finite rate (because of transport and kinetic limitations) spreads the cooling effect along the anode and reduces the temperature drop at the inlet. Second, radiant heat transfer is significant at the high temperatures of operation of the SOFC. The radiant heat transfer between two surfaces of temperature  $T_1$  and  $T_2$  is proportional to  $T_1^4 - T_2^4$ . Radiant heat transfer will tend to equalize temperatures along the length of the fuel cell.

The model is being extended to include the effect of finite reform rates and radiant heat transfer on cell performance.

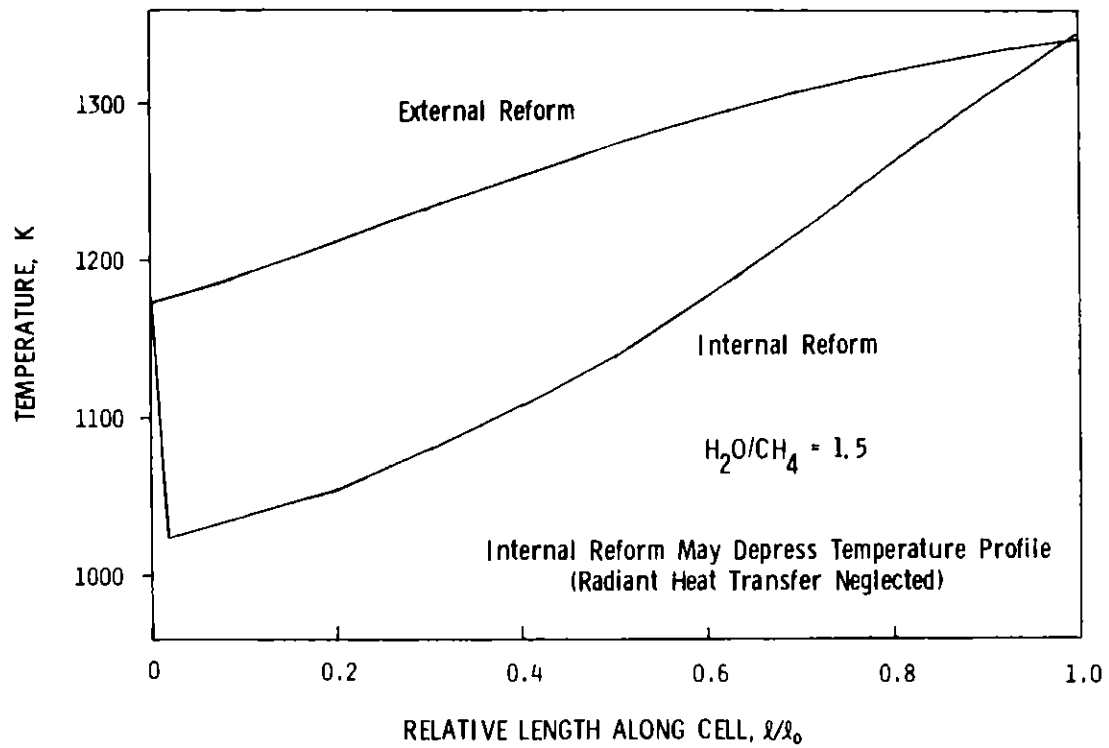


Fig. 33. Temperature Profile along the Length of a Solid Oxide Fuel Cell (85% fuel utilization)

## REFERENCES

1. T. D. Claar, R. A. Donado, and L. G. Marianowski, The Effects of Sulfur Containing Gases on MCFC Behavior, Proceedings of the DOE/EPRI Workshop on Molten Carbonate Fuel Cells, Electric Power Research Institute Report EPRI-WS-78-135, pp. 5-5 through 5-20 (November 1979).
2. S. W. Smith, L. J. Bregoli, and W. M. Vogel, Molten Carbonate Cell Sulfur Tolerance, Proceedings of the DOE/EPRI Workshop on Molten Carbonate Fuel Cells, Electric Power Research Institute Report EPRI-WS-78-135, p. 5-21 (November 1979).



Distribution for ANL-84-64Internal:

J. P. Ackerman	T. D. Kaun	J. L. Smith
P. A. Blackburn	V. M. Kolba	J. R. Stapay
R. L. Breyne	T. E. Kraft	M. J. Steindler
T. D. Claar	M. Krumpelt	R. K. Steunenber
G. M. Cook	G. H. Kucera	B. S. Tani
D. W. Dees	N. Q. Minh	E. H. VanDeventer
J. T. Dusek	F. C. Mrazek	J. E. Young
D. C. Fee	Z. Nagy	S. A. Zwick
P. A. Finn	P. A. Nelson	A. B. Krisciunas
B. K. Flandermeyer	J. J. Picciolo	ANL Patent Dept.
A. V. Fraioli	R. D. Pierce (25)	ANL Contract File
J. E. Harmon	R. B. Poeppel	ANL Libraries (3)
A. A. Jonke	J. J. Roberts	TIS Files (6)

External:

DOE-TIC, for distribution per UC-93 (138)

Manager, Chicago Operations Office, DOE

R. J. Gariboldi, DOE-CH

Chemical Technology Division Review Committee Members:

S. Baron, Brookhaven National Lab.

W. L. Worrell, U. Pennsylvania

E. B. Yeager, Case Western Reserve U.

Materials Science and Technology Division Review Committee:

C. B. Alcock, U. Toronto

A. Arrott, Simon Fraser U.

R. C. Dynes, Bell Labs., Murray Hill

A. G. Evans, U. California, Berkeley

H. K. Forsen, Bechtel National, Inc., San Francisco

E. Kay, IBM San Jose Research Lab.

M. B. Maple, U. California-San Diego

P. G. Shewmon, Ohio State U.

J. K. Tien, Columbia U.

J. W. Wilkins, Cornell U.

B. S. Baker, Energy Research Corp., Danbury, Conn.

L. J. Bates, Battelle Pacific Northwest Lab.

T. R. Beck, Electrochemical Technology Corp., Seattle

A. Boni, Physical Sciences, Inc., Andover, Mass.

R. Bradley, Oak Ridge National Lab.

E. Camara, Inst. Gas Technology, Chicago

P. T. Carlson, Oak Ridge National Lab.

T. W. Carter, U. S. Coast Guard, Washington

J. Cuttica, Gas Research Inst., Chicago

W. Feduska, Westinghouse R&D Center, Pittsburgh

L. M. Ferris, Oak Ridge National Lab.

A. P. Fickett, Electric Power Research Inst., Palo Alto

E. Gillis, Electric Power Research Inst., Palo Alto

J. Giner, Giner, Inc., Waltham, Mass.

F. Gmeindl, Morgantown Energy Technology Center, USDOE

G. L. Hagey, Div. Advanced Energy Conversion Systems, USDOE

L. C. Headley, Morgantown Energy Technology Center, USDOE

D. T. Hooie, Gas Research Inst., Chicago  
W. Huber, Morgantown Energy Technology Center, USDOE  
A. O. Isenberg, Westinghouse R&D Center, Pittsburgh  
B. Jackson, Tennessee Valley Authority, Chattanooga  
D. Jewell, Morgantown Energy Technology Center, USDOE  
D. Johnson, Northwestern U.  
C. Kinney, Office of Fossil Energy, USDOE  
K. Kinoshita, Lawrence Berkeley Lab.  
M. Kresge, Mitsubishi International Corp., New York City  
H. R. Kunz, United Technologies Corp., South Windsor, Conn.  
A. R. Maret, Gas Research Inst., Chicago  
N. Margalit, Combustion Engineering, Windsor  
L. Marianowski, Inst. of Gas Technology, Chicago  
H. Maru, Energy Research Corp., Danbury, Conn.  
R. Matsumoto, Ceramatech, Salt Lake City  
A. P. Meyer, United Technologies Corp., South Windsor, Conn.  
C. A. Reiser, United Technologies Corp., South Windsor, Conn.  
F. Salzano, Brookhaven National Lab.  
J. Searls, U. S. Bureau of Mines, Washington  
J. R. Selman, Illinois Inst. of Technology  
J. Sholes, Morgantown Energy Technology Center, USDOE  
P. Stonehart, Stonehart Associates, Inc., Madison, Conn.  
G. Wilemski, Physical Sciences Inc., Andover, Mass.  
C. Zeh, Morgantown Energy Technology Center, USDOE